Geochemistry, Geophysics, Geosystems

RESEARCH ARTICLE
10.1029/2020GC009156

Key Points:

- Multitracer provenance study offshore central Wilkes Land, East Antarctica, supports former interpretations of the subglacial geology
- Age and composition of the detritus matches basement rocks of the proximal onshore Wilkes, Nuyina, and Banzare provinces
- Changes in detrital sediment provenance over c. 23.5 ka are associated with variation in climate and ice sheet configuration

Supporting Information:

- Supporting Information S1
- Figure S1
- Figure S2

Correspondence to:

S. Tooze,
sian.tooze@utas.edu.au

Citation:

Tooze, S., Halpin, J. A., Noble, T. L., Chase, Z., O'Brien, P. E., & Armand, L. (2020). Scratching the surface: A marine sediment provenance record from the continental slope of central Wilkes Land, East Antarctica. *Geochemistry, Geophysics, Geosystems*, *21*, e2020GC009156. https://doi.org/10.1029/2020GC009156

Received 4 MAY 2020
Accepted 30 SEP 2020

Scratching the Surface: A Marine Sediment Provenance Record From the Continental Slope of Central Wilkes Land, East Antarctica

Sian Tooze[1], Jacqueline A. Halpin[1], Taryn L. Noble[1], Zanna Chase[1], Philip E. O'Brien[2], and Leanne Armand[3]

[1]Institute for Marine and Antarctic Studies, University of Tasmania, Hobart, TAS, Australia, [2]Macquarie University, Sydney, NSW, Australia, [3]The Research School of Earth Sciences, The Australian National University, Canberra, ACT, Australia

Abstract The geology of Wilkes Land, East Antarctica, is masked by kilometers of ice and remains largely unexplored. Defining the sediment provenance adjacent to this hidden region is important for distinguishing the proximal subglacial basement terranes and refining the dynamic regional glaciological history. This study presents a detrital sediment provenance record spanning c. 23.5 ka from the continental slope of central Wilkes Land. Sediment provenance was characterized using U-Pb geochronology and trace element geochemistry from detrital zircon, titanite and apatite, and Pb isotopic signatures from detrital feldspar. These data were compared with new feldspar Pb-isotopic signatures and existing U-Pb zircon data sets from rare nearby coastal outcrop. A principally igneous source was revealed with dominant age populations between c. 1,360-1,100 Ma and c. 1,620-1,490 Ma, characteristic of rocks of the proximal Wilkes and Banzare provinces, respectively. Minor detritus was additionally sourced from the proximal Nuyina Province (c. 1,450-1,390 Ma). Temporal variation in the climate and ice sheet configuration are likely responsible for subtle downcore changes observed in detrital sediment provenance. High sedimentation rates during the glacial period suggest reworking of continental shelf sediments and downslope transport in debris flows during ice sheet advance. Glacial meltwater fluxes fed largely by the Totten Glacier were responsible for supplying detritus during deglaciation. During interglacials, detritus was derived from a broad coastal region and delivered to the slope via multiple glacial outlets. These results present the first substantial offshore evidence to support recent interpretations that the subglacial crust of central Wilkes Land has a dominantly Mesoproterozoic history.

Plain Language Summary The geology underlying the Antarctic ice cap is poorly known due to thick and extensive ice cover. Understanding the composition of the rock types beneath the ice and how they are eroded and transported to the ocean is important for establishing the regional glaciological and tectonic histories. This study analyzes the age and composition of grains in marine sediment originally eroded from Wilkes Land, East Antarctica, to determine the source rock type, age, and likely provenance region. The composition of detritus is compared to that of nearby coastal rocks and the geology of southern Australia that was once adjacent to East Antarctica during past supercontinents. The detrital composition and age signature match the proximal Banzare, Nuyina, and Wilkes provinces in East Antarctica, validating the use of marine sediment records as a window into the hidden Antarctic bedrock. During glacial periods, detritus was scoured from the continental shelf and redeposited downslope. As the ice sheet began to retreat, fluxes of sediment-laden meltwater were largely supplied by Totten Glacier. Detritus is sourced from a broad region of the coast during warm interglacials. This record provides the first substantial physical evidence to support former interpretations of the subglacial terrain in central Wilkes Land.

1. Introduction

The subglacial geology of Wilkes Land, East Antarctica, is poorly characterized, due to its concealment beneath 0.4–4 km of thick ice (Fretwell et al., 2013) with sparse coastal rock outcrop. Yet, a better understanding of the ice-covered continental crust has the potential to provide valuable insights into the dynamic tectonic history of East Antarctica and its role during supercontinent cycles (e.g., Aitken et al., 2016a;

Mulder et al., 2019). Additionally, deciphering the bedrock composition can help identify sediment erosion and transport pathways and constrain subglacial conditions (e.g., geothermal heat flow, topography, and basal erosion) deemed to have impacted Antarctic Ice Sheet evolution (Golledge et al., 2013; Jamieson et al., 2010; Lowry et al., 2020). In this context, the Sabrina Subglacial Basin in Wilkes Land (Aitken et al., 2016b; Figure 1a) is of particular interest, forming part of an extensive glacial drainage system that is predominantly situated below sea-level (Fretwell et al., 2013; Young et al., 2011). This region drains into the ocean via the rapidly retreating Totten Glacier (Rignot et al., 2019; Figure 1b) and has the capacity to raise global sea-level by 3.5 m (Greenbaum et al., 2015).

Multiple sedimentary features of the continental slope of the Sabrina Coast provide evidence for sediment delivery via meltwater fluxes supplied by major glacier systems throughout the Late Cenozoic (c. 34 Ma to present; Donda et al., 2020). The Totten Glacier is considered to have played a central role in controlling these sediment-laden meltwater fluxes that have historically shaped the submarine landscape. The slope bathymetry in this region is characterized by two large contourite ridges to the west and a dendritic network of gullies that develop into submarine canyons to the east (O'Brien et al., 2020; Post et al., 2020; Figure 1a). These sedimentary features have been observed and interpreted in other regions around East Antarctica (e.g., De Santis et al., 2007; Donda et al., 2020; O'Brien et al., 2016) and West Antarctica (Amblas & Canals, 2016; Dowdeswell et al., 2004, 2006; Gales et al., 2013) and provide records of sediment erosion during the evolution of the ice sheet.

Studies of marine sediment provenance around Antarctica have been used to investigate the subglacial terrain in the absence of onshore geological data and to complement nonunique geophysical signatures (Licht & Hemming, 2017; Pierce et al., 2014; Roy et al., 2007; Williams et al., 2010). In this study, we aim to test existing interpretations of subglacial bedrock composition and erosion pathways in central Wilkes Land. We do this by characterizing the isotopic and geochemical signature of detrital grains in a sediment core recovered from the eastern flank of a large contourite ridge situated on the continental slope of the Sabrina Coast in central Wilkes Land (Figure 1a).

2. Background: A Brief Glaciological and Geological History of Wilkes Land

Our interpretation of the composition, provenance, and transport of continentally derived detritus from Antarctica is informed by current understanding of the temporal changes to the Antarctic Ice Sheet and the regional geological history. Here, we provide a brief synopsis of the East Antarctic Ice Sheet configuration from its maximum extent during the last glacial period to present, followed by a summary of the geological evolution of central Wilkes Land, East Antarctica.

2.1. Evolution of the East Antarctic Ice Sheet from the Late Pleistocene to Present

The expansion and retreat of the ice sheet over glacial to interglacial timescales has left an imprint on the sedimentary basin infill in central Wilkes Land (Aitken et al., 2016b). Region A of the Sabrina Sedimentary Basin (Figure 1a), is characterized by a thin subglacial sedimentary rock veneer (<1 km in thickness), in some places exposing crystalline basement rock at the base of the ice sheet (Aitken et al., 2016b). The scarcity of sedimentary rock between the base of the ice sheet and basement geology is interpreted as indicating repeated erosion during cyclic waxing and waning of the ice sheet in this region (Aitken et al., 2016b). Ancient shelf sedimentary megasequences provide additional evidence of repeated ice sheet advance and retreat from the beginning of the Oligocene to the mid-Miocene (Gulick et al., 2017).

Sedimentary bedforms on the continental shelf and slope of central Wilkes Land also preserve a dynamic history of sediment erosion, transport, and deposition. Throughout the Late Cenozoic (phases 2–4 of Donda et al., 2007), the East Antarctic Ice Sheet was unstable and sediment-laden meltwater fluxes sourced from major outlet glaciers (Figure 1b) had an important influence on the morphology of the seabed on the continental shelf, slope, and rise (Donda et al., 2007; Leitchenkov, 2015). In the west of the study region, large sediment contourites formed on the continental slope and are maintained by debris flows and fallout from sediment-rich meltwater plumes (Donda et al., 2020; O'Brien et al., 2020). Donda et al. (2020) suggested that the proximal Totten Glacier likely supplies a significant component of detritus to the slope in sediment-laden meltwater fluxes, maintaining these submarine landforms. Gullies developed in the east of

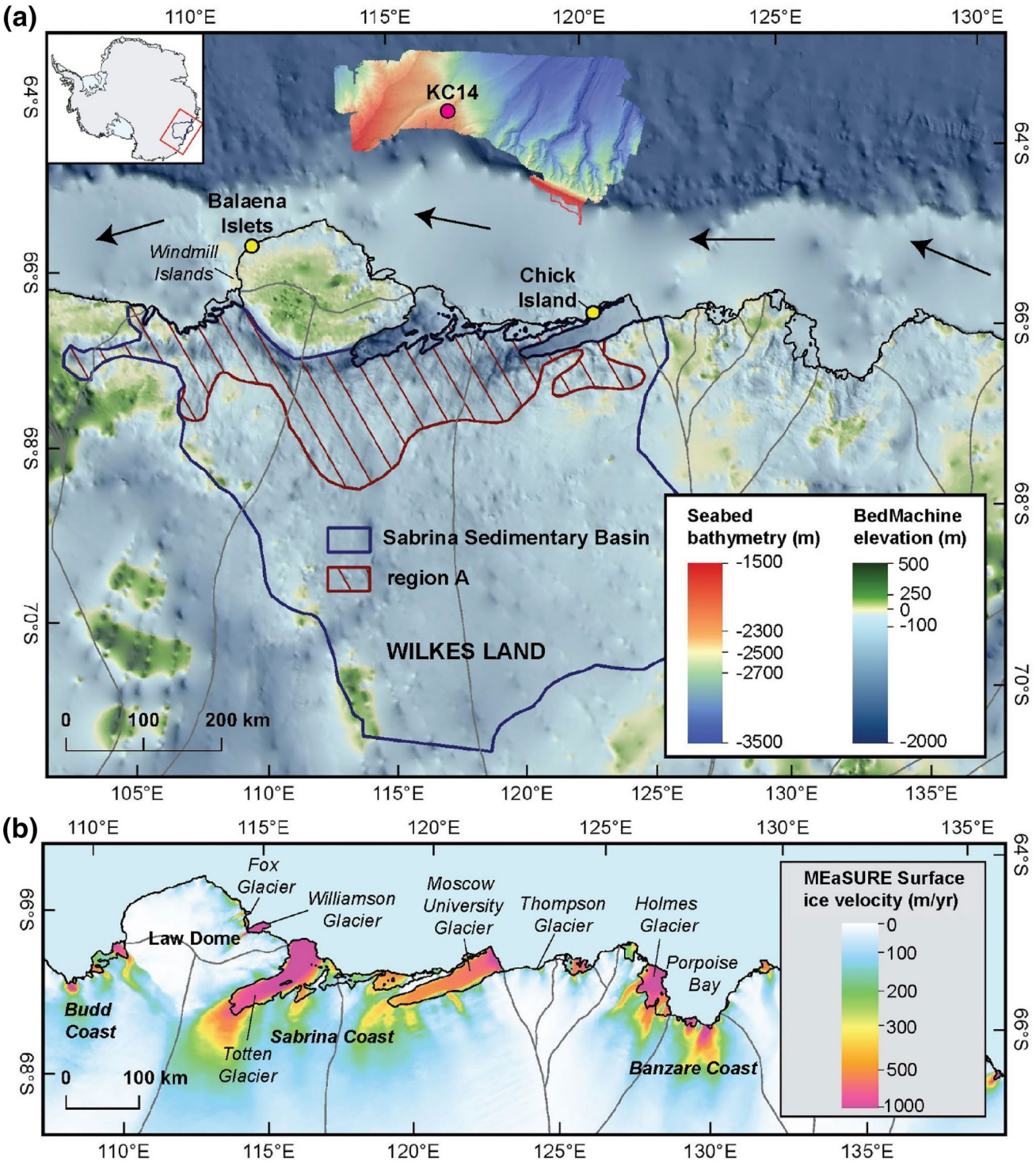

Figure 1. (a) Map of central Wilkes Land, East Antarctica, with coastal (yellow) and offshore (pink) sample locations. Bed elevation is the BedMachine model of Morlighem et al. (2020). High-resolution bathymetry of the continental slope was acquired from *RV Investigator* (voyage IN2017_V01; Armand et al., 2018) and of the continental shelf from the *RV Nathaniel B. Palmer* (voyage NBP1402; Fernandez et al., 2018). Simplified outline of the Sabrina Sedimentary Basin (bold dark blue line) is from Maritati et al. (2019) after Aitken et al. (2016b). Region A, an area of thin sedimentary rock cover (<1-km thick) and basement rock exposure is interpreted by Aitken et al. (2016b). Gray lines mark the boundaries of ice drainage basins (Mouginot et al., 2017). Black arrows represent the westward-flowing Antarctic Coastal Current. Inset shows the study location (red box) on a map of Antarctica. (b) MEaSUREs surface ice velocity from InSAR data, highlighting major glacier outflows in central Wilkes Land (Mouginot et al., 2012; Rignot et al., 2011).

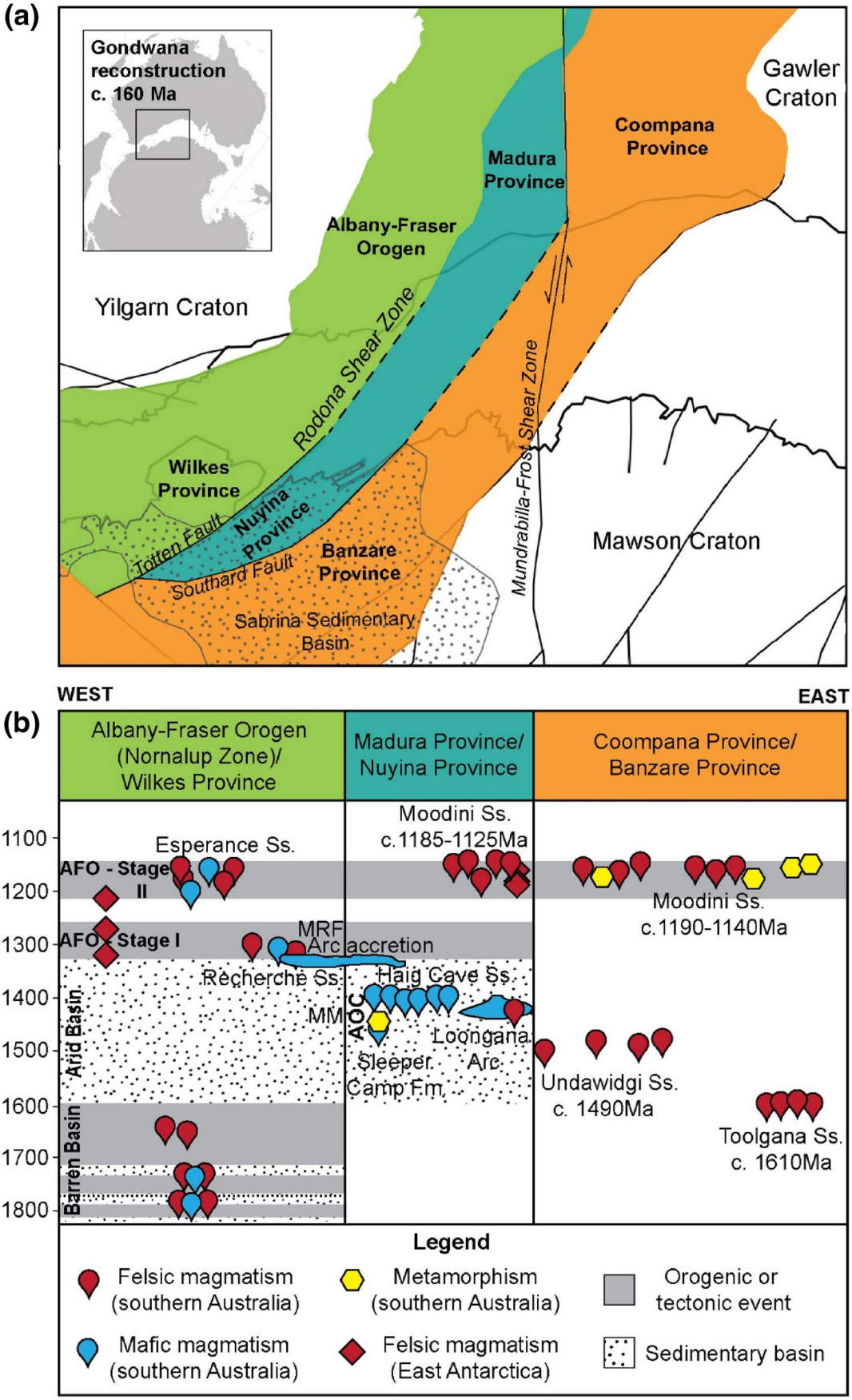
(a)
Gondwana reconstruction c. 160 Ma
Gawler Craton
Coompana Province
Madura Province
Albany-Fraser Orogen
Yilgarn Craton
Rodona Shear Zone
Mundrabilla-Frost Shear Zone
Wilkes Province
Nuyina Province
Totten Fault
Southard Fault
Banzare Province
Sabrina Sedimentary Basin
Mawson Craton
(b)
WEST
EAST
Albany-Fraser Orogen (Nornalup Zone)/ Wilkes Province
Madura Province/ Nuyina Province
Coompana Province/ Banzare Province
Age (Ma)
1100
1200
1300
1400
1500
1600
1700
1800
Esperance Ss.
AFO - Stage II
AFO - Stage I
MRF
Arc accretion
Recherche Ss.
Haig Cave Ss.
MM
AOC
Loongana Arc
Sleeper Camp Fm.
Arid Basin
Barren Basin
Moodini Ss. c.1185-1125Ma
Moodini Ss. c.1190-1140Ma
Undawidgi Ss. c. 1490Ma
Toolgana Ss. c. 1610Ma
Legend
Felsic magmatism (southern Australia)
Metamorphism (southern Australia)
Orogenic or tectonic event
Mafic magmatism (southern Australia)
Felsic magmatism (East Antarctica)
Sedimentary basin

the study region, where turbidite flows and meltwater fed by major glacial systems scoured into the seabed (Donda et al., 2020; O'Brien et al., 2020; Post et al., 2020).

Previous studies on the continental shelf of the Sabrina Coast provide evidence for maximum expansion of the ice sheet to within 2–5 km of the shelf break during past glaciations (Fernandez et al., 2018; Post et al., 2020), but uncertainty remains around the exact position of the maximum grounding line extent. During the last glacial period, as the ice sheet expanded close to the edge of the present-day continental shelf, the advancing ice remobilized sediments on the continental shelf and redeposited them on the continental slope (Post et al., 2020). As the ice sheet retreated, rising sea-level and sea-surface temperatures in the Southern Ocean promoted iceberg calving and meltwater production (Weber et al., 2014). The supply of detritus to the continental slope during deglaciation was controlled by erosion at the base of the grounded ice sheet, and the release of englacial debris in meltwater plumes (Donda et al., 2020; O'Brien et al., 2020).

2.2. The Subglacial Geology of Central Wilkes Land

Throughout successive periods of supercontinent assembly (e.g., Nuna, Rodinia, and Gondwana), much of the East Antarctic and southern Australian lithosphere accreted and consolidated forming a contiguous Australo-Antarctic component (e.g., Aitken et al., 2016a; Boger, 2011; Fitzsimons, 2003). This ancient tectonic relationship has cemented strong geological and structural affinities between the two now conjugate margins (Williams et al., 2019). Hampering our understanding, the basement rock geology is concealed under sedimentary basins and regolith in southern Australia and thick ice in East Antarctica. Existing interpretations in Wilkes Land rely on analysis of rare coastal rock outcrop (e.g., Maritati et al., 2019; Morrissey et al., 2017; Mulder et al., 2019; Tucker et al., 2017) combined with borehole analyses from southern Australia (e.g., Kirkland et al., 2017; Wingate et al., 2015a) and airborne geophysical data (Aitken et al., 2014). From west to east, three geologically distinct Mesoproterozoic provinces have been identified using these methods: the Albany-Fraser Orogen (c. 1,300-1,140 Ma), Madura Province (c. 1,475-1,390 Ma), and Coompana Province (c. 1,610-1,490 Ma); their Antarctic equivalents defined as the Wilkes, Nuyina, and Banzare provinces, respectively (e.g., Aitken et al., 2014; Fitzsimons, 2003; Maritati et al., 2019). The geological relationships between southern Australia and East Antarctica are summarized below (Figure 2) to provide context for our provenance analysis. A more comprehensive regional geological history can be found in the references herein.

The Albany-Fraser Orogen (Figure 2) is characterized by reworked Archean and Proterozoic crust (Spaggiari et al., 2015). Exposed metasedimentary rocks of the Windmill Islands (Figure 1) within the Wilkes Province in East Antarctica compare to those of the Mount Ragged Formation (Clark et al., 2000) in the Albany-Fraser Orogen, on the basis of shared detrital U-Pb age signatures (Fitzsimons, 2003; Morrissey et al., 2017). Granite and charnockite intrusions in the Windmill Islands in East Antarctica have crystallization ages between c. 1,325-1,170 Ma, coeval with the Recherche (c. 1,300-1,290 Ma, Nelson et al., 1995) and Esperance (c. 1,200-1,140 Ma, Nelson et al., 1995) supersuites of the Nornalup Zone, the easternmost zone of the Albany-Fraser Orogen (Morrissey et al., 2017). The Rodona Shear Zone in southern Australia (Figure 2a) is interpreted to be equivalent to the Totten Fault (of Aitken et al., 2014; Figure 2a) underlying the Totten Glacier, marking the suture zone between the continental crust of the Albany-Fraser Orogen/Wilkes Province to the west and the oceanic crust of the Madura/Nuyina Province to the east (Maritati et al., 2019; Spaggiari et al., 2018).

The Madura and Coompana provinces have been distinguished geophysically (Aitken et al., 2014). Low magnetic intensities are representative of the c. 1610 Ma Toolgana and c. 1490 Ma Undawidgi supersuites of the Coompana Province and are distinct from the high magnetic intensities of the c. 1,190-1,140 Ma Moodini Supersuite that intrudes both the Madura and Coompana provinces (Kirkland et al., 2017). Comparable geophysical signatures for these three igneous supersuites are also identified in central Wilkes Land (Aitken et al., 2014; Maritati et al., 2019). Outcrop is very sparse in this region although recent zircon U-Pb-Hf geochronol-

Figure 2. Geological provinces of southern Australia and East Antarctica. (a) Full-fit Gondwana tectonic reconstruction at c. 160 Ma with Antarctica fixed in its present-day reference frame (Matthews et al., 2016). Larger-scale geographic location is shown in the inset. Geological provinces in southern Australia and conjugate regions of East Antarctica shown using most recent interpretation of Maritati et al. (2019). Fault positions are after Aitken et al. (2014) and Maritati et al. (2019). (b) Time-space diagram with geological provinces of southern Australia and their Antarctic counterparts shown from west to east. Key magmatic and metamorphic events associated with the formation of provinces are interpreted from U-Pb analyses of in-situ zircon from basement rocks. Data from southern Australia are from Wingate et al. (2015a, 2015b) and data from East Antarctica are from Maritati et al. (2019) and Morrissey et al. (2017). AOC, Arubiddy ophiolite complex; MM, Malcolm Metamorphics; MRF, mount ragged formation; Ss., supersuite. Ages and spatial positions are approximate.

ogy undertaken on basement igneous samples from Chick Island (Figure 1) reveal c. 1,150 Ma granodioritic plutons with affinity to the Moodini Supersuite (Maritati et al., 2019). Furthermore, older c. 1,530-1,290 Ma xenocrystic zircon grains yield U-Pb-Hf signatures that correlate with older magmatic suites within both the Madura and Coompana provinces, suggesting that Chick Island lies close to the boundary between the Nuyina and Banzare provinces in East Antarctica (Maritati et al., 2019; Figure 2a). The crystalline basement rocks of the Coompana Province in Australia are overlain by two large sedimentary basins: the Neoproterozoic-Devonian Officer Basin and the Cretaceous-Tertiary Eucla Basin, the former of which has been recently correlated with the East Antarctic Sabrina Sedimentary Basin (coincident with the Sabrina Subglacial Basin) based on zircon U-Pb-Hf analyses from Neoproterozoic-aged sandstone erratics discharged from the Vanderford Glacier and found in the vicinity of the Windmill Islands (Maritati et al., 2019).

3. Methods

3.1. Sampling Locations and Descriptions

We report results from a marine sediment core recovered from the continental slope adjacent to Sabrina Coast of central Wilkes Land, East Antarctica, and nearby basement rocks (Figure 1 and Table S1). Core IN2017_V01-A042-KC14 (hereafter referred to as KC14) was recovered in 2017 employing a 15-cm^2 Kasten corer from aboard the *RV Investigator* (Armand et al., 2018). KC14 was targeted for this study due to its proximity to Totten Glacier and its continuous sequence of sediment deposition. The core is 3.38-m long and was recovered from the eastern flank of a large contourite ridge 2,100 m below sea level. The core sedimentology consists predominantly of glacigenic clay and silty clay overlain by biosiliceous silty clay in the Holocene (Armand et al., 2018). To complement the offshore samples, the nearest onshore basement rocks from Chick Island (Maritati et al., 2019) and Balaena Islets (Cameron et al., 1958) were sampled for feldspar Pb isotope analysis.

3.2. Radiocarbon Dating

The bulk acid-insoluble organic carbon fraction of six samples from KC14 was radiocarbon-dated. Prior to dating, all samples (weighing ~5 g) were dried in an oven at 60°C, ground and submerged in 2M HCl for several hours on a hotblock at 80°C for carbonate removal. Each sample was subsequently rinsed with Milli-Q water to remove any residual acid and dried at 60°C. Radiocarbon analysis by Accelerator Mass Spectrometry was performed by DirectAMS. The raw age data were corrected for the Marine Reservoir Effect and calibrated using the Marine13 calibration curve in MatCal 2.41 (Lougheed & Obrochta, 2016). A uniform marine reservoir age of 917.5 ± 30 year was applied as this is the median of the range of reservoir ages currently defined for the Southern Ocean (Paterne et al., 2019). Median calibrated ages are reported with a 95% confidence limit.

3.3. Quantification of Iceberg-Rafted Debris Flux

Iceberg-rafted debris (IBRD) flux was calculated at 10 cm intervals along the core following the protocol of Krissek (1995) and Patterson et al. (2014):

$$\mathrm{IBRD}_{\mathrm{flux}} = \mathrm{CSF} \times \mathrm{DBD}\left(\mathrm{g}/\mathrm{cm}^3\right) \times \mathrm{LSR}\left(\mathrm{cm}/\mathrm{Kyr}\right)$$

The coarse sand fraction (CSF; 250 μm–2 mm) was isolated by wet-sieving a known weight of each sample. Authigenic grains and microfossils were removed from the samples under a microscope. The remaining material was weighed on a microbalance and calculated as a fraction of the bulk sample. Cuvettes with a precise volume of 5.49 cm^3 were used to calculate the dry bulk density (DBD). The linear sedimentation rate (LSR) was calculated at intervals between the calibrated bulk organic carbon ages.

3.4. Biogenic Silica Concentrations

Biogenic silica concentrations were measured at 10-cm intervals along KC14 following a protocol based on DeMaster (1981) and Mortlock and Froelich (1989). Samples (30 ± 3 mg) were leached in 30-mL 1M $NaCaO_3$ solution and maintained at 85°C on a hotblock. After 1 h, a 1-mL aliquot was centrifuged at 10,000 rpm for 45 s to separate the sediment from the leached biogenic silica. A 200-μL aliquot of the solution was

then diluted in 9 mL of Milli-Q water and the dissolved silica was analyzed immediately using a Quickchem 8500 Series 2 FIA (Method 31-114-27-1-A, Diamond, 2002). This process was repeated for a total of 5 h. The biogenic silica in all samples was fully leached after 3 h. The percent standard deviation of two replicate analyses of in-house sediment standards, over a 2-day period, was 15% and 7%, respectively, for an Antarctic margin (Collaborative East Antarctic Marine Census) standard (15.2% biogenic silica) and a Chile margin sediment standard (6.6% biogenic silica). The biogenic silica flux was calculated in the same way as the IBRD flux, replacing the CSF with the biogenic silica mass fraction from each sample.

3.5. Trace Element, U-Pb, and Pb-Pb Analysis

3.5.1. Sample Preparation

The fine (<63 μm), intermediate (63–250 μm), and coarse (>250 μm–2 mm) fractions were acquired from 2-cm-thick sediment samples (weighing ~20 g) at 10-cm intervals along KC14 by wet-sieving. For subsequent analysis and interpretation, all the sampled 10-cm intervals were used from the intermediate size fraction, supplemented by four samples at ~1-m intervals from each of the coarse and fine fractions. In the fine fraction, detrital grains were separated from clay minerals and subsequently mounted in resin. In the intermediate fraction, the heavy and light mineral fractions were manually separated by suspending the grains in Milli-Q water and rotating them around a watchglass. Nonmagnetic and weakly magnetic grains were then separated from the dried heavy mineral fraction using a Fe-B-Nd hand magnet and mounted in epoxy resin. For the coarse fraction, the CSF samples used to calculate the IBRD flux were mounted in epoxy resin. The one-inch-round resin discs were then sanded and polished to expose the interior of the grains. Basement rock samples were similarly prepared with rock chips from each sample mounted in resin before being dried and polished.

3.5.2. Sample Imaging

Sample mounts were imaged and analyzed on a FEI MLA650 environmental scanning electron microscope at the Central Science Laboratory, University of Tasmania (UTAS). Using Mineral Liberation Analysis (MLA) software, all mineral types in each mount were identified and color-coded using a predefined mineral library. In this way, detrital zircon, apatite, titanite, K-feldspar, and plagioclase feldspar from KC14, and K-feldspar and plagioclase feldspar from the four basement samples, were located in preparation for Laser Ablation-Inductively Coupled Plasma Mass Spectrometry (LA-ICPMS). Where possible, high-resolution backscatter and cathodoluminescence (CL) images of zircons from the intermediate (63–250 μm) fraction were acquired, capturing the external morphology, internal structure and zoning of the grains, and identifying optimal sites for LA-ICPMS analysis. Elongation ratios (length:width) for imaged zircons were quantified using the MLA software. The detrital titanite, apatite, and feldspar grain morphologies were examined under a microscope.

3.5.3. LA-ICPMS Analysis

LA-ICPMS measurements were made using an ASI Resolution S-155 System with a large format cell and a Coherent CompexPro 110 Excimer laser coupled with an Agilent 7900 ICPMS at the Discipline of Earth Sciences/Centre of Ore Deposit and Earth Sciences (CODES), UTAS. Specific instrumental parameters and standard reference materials used are listed in Table S2. Detrital zircon, apatite, and titanite were targeted from all size fractions for U-Pb analysis. Detrital plagioclase and K-feldspars were selected from the CSF only for Pb-Pb analysis.

The experimental setup for U-Pb and trace element analysis of zircon, apatite, and titanite follows Thompson et al. (2018). A glass primary standard, NIST610, was used to calculate a correction factor for the 207Pb/206Pb ratio using values proposed by Baker et al. (2004). Primary standard 91500 (Horstwood et al., 2016) was used for the calibration of all U-Pb ratios in zircon, with Plešovice (Sláma et al., 2008) and Temora (Black et al., 2003) used as secondary reference materials and treated as unknowns. During the analysis of apatite, OD306 (Thompson et al., 2016) was used as a primary standard and Otter Lake (Barfod et al., 2005), Emerald Lake (Coulson et al., 2002), 401 apatite (Thompson et al., 2016), McClure Mountain (Schoene & Bowring, 2006), and Durango (McDowell et al., 2005) as secondary reference materials. An in-house primary standard, 19686-titanite, was used for titanite analysis with Mt. Dromedary (Miller et al., 1985) and FC-3 (Schmitz & Bowring, 2001) as secondary reference materials.

Initial U-Pb-trace element data reduction follows Thompson et al. (2018) and Halpin et al. (2014) using Microsoft Excel macro spreadsheets created at the UTAS. Following these data reduction steps, we filtered the zircon data set to exclude: (1) processed signal intervals spanning less than 50% of the overall analysis time, (2) high ^{204}Pb values exceeding 100 cps, (3) concordance outside the range 80%–110%, and (4) grains displaying high Light Rare Earth Element (LREE) and P-contents ($n = 15$) symptomatic of mixed ablation of apatite or monazite microinclusions. A total of 139 analyses (44% of the data set) were eliminated using these criteria and were excluded from interpretation. All rare earth element (REE) data were chondrite-normalized using values proposed by Sun and McDonough (1989). A common-Pb correction procedure was applied for the detrital apatite and titanite U-Pb-trace element data sets, which were discordant due to common Pb. We followed the five-stage iterative 207Pb-correction method of Chew et al. (2011), with estimates of initial Pb-isotopic compositions from the Stacey and Kramers (1975) crustal Pb evolution model. Some analyses recorded significant differences in the calculated ^{207}Pb-corrected ^{206}Pb/^{238}U ages after the fifth iteration. To account for this, the uncertainty for common Pb on all analyses was increased using the absolute difference in the common Pb predicted by the fourth and fifth iterations. Subsequent to this common Pb correction procedure, we further filtered the apatite and titanite data set to exclude processed signal intervals spanning less than 50% of the total analysis time, which eliminated 22% and 10% of the apatite and titanite data sets, respectively. Probability-density plots were produced using DensityPlotter version 8.4 (Vermeesch, 2018). For zircon, ^{207}Pb-corrected ^{206}Pb/^{238}U ages were used for grains with ^{207}Pb/^{206}Pb ages younger than 1,000 Ma ($n = 9$) and showing no evidence of Pb loss, and ^{207}Pb/^{206}Pb ages were used for the remainder (>1,000 Ma; 95% of the data set). For apatite and titanite, plotted ages are fifth iteration ^{207}Pb-corrected ^{206}Pb/^{238}U ages. Tera-Wasserburg plots (Figure S1) were constructed using IsoplotR (Vermeesch, 2018).

A comprehensive description of the method used for Pb-Pb analysis of detrital feldspar using the UTAS LA-ICPMS system is given by Mulder et al. (2019). Lines, rather than spots, were used for feldspar ablation to maintain the signal intensity and smooth, unaltered areas of individual grains were targeted for analysis. Data reduction also followed Mulder et al. (2019); only one analysis with a signal less than 50% of the total analysis time was excluded from interpretation. No correction for the in-growth of radiogenic Pb was applied due to the avoidance of U and Th inclusions. NIST612 was ablated for the calibration of all Pb-Pb ratios, using values proposed by Baker et al. (2004) and glass reference materials GSD-1g (Jochum et al., 2011) and BCR-2g (Jochum et al., 2016) were used as secondary standards and treated as unknowns. No feldspar reference standard was available during this study, however, the UTAS facility uses glass reference materials for Pb-isotopic compositions on a wide range of minerals without a measurable "matrix effect" on the quadrupole ICPMS system (e.g., monazite: Berry et al., 2016; pyrite: Hawke et al., 2015; zircon: Thompson et al., 2018).

Weighted average values for all LA-ICPMS standards were calculated using the Microsoft Excel add-in Isoplot v. 4.15 (Ludwig, 2012), all of which fall within 2σ error of the published reference values (Table S3).

4. Results

4.1. Bulk Organic Carbon Ages, IBRD Flux, and Biogenic Silica Concentrations

The median calibrated calendar ages for KC14 capture a Quaternary record spanning c. 23,500 cal years BP. Based on the bulk radiocarbon ages and low biogenic silica concentrations (representing low productivity characteristic of glacial conditions), the base of the core to 170 cm represents the last glacial period (interval 4, Figure 3). At 170 cm, biogenic silica concentrations start to increase, indicating increased productivity, which we infer represents the deglaciation and a transition into the Holocene (interval 3, Figure 3). Estimated LSRs were highest during the glacial (377 cm/Kyr) and moderate in the Holocene (10–11 cm/Kyr). A sharp decline in the LSR to 8 cm/Kyr followed by an increase to 14 cm/Kyr marks the deglacial transition between the last glacial period and the Holocene (Figure 3). The CSF ranges between 0.0001 and 0.0147, with an average of 0.003 in the glacial and 0.001 in the Holocene (Figure 3). The biogenic silica flux averages 7.6 g/cm^2/Kyr in the glacial and 2.0 g/cm^2/Kyr in the Holocene and positively correlates with the IBRD flux. The IBRD flux ranges between 0.001 and 3.4 g/cm^2/Kyr with an average of 0.4 g/cm^2/Kyr during the glacial period and 0.004 g/cm^2/Kyr during the Holocene (Figure 3).

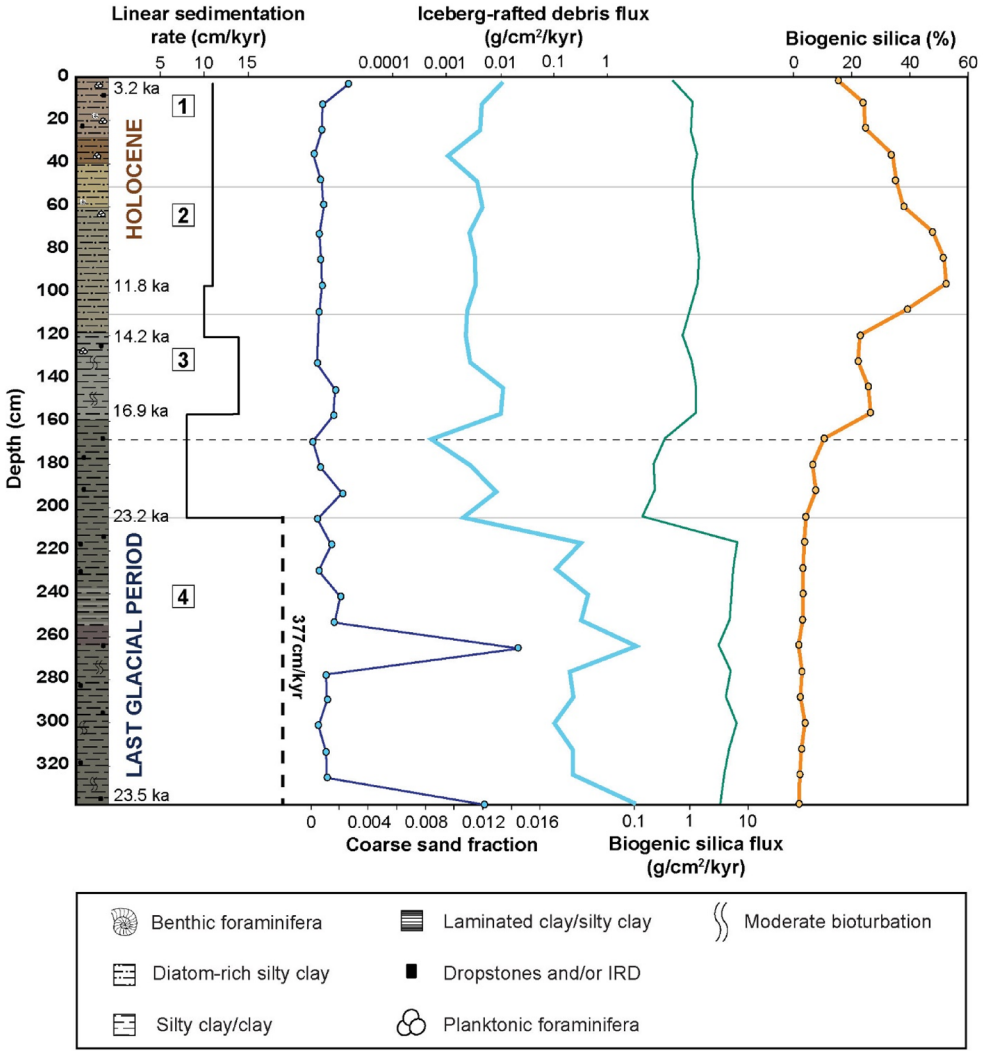

Figure 3. KC14 downcore calibrated bulk organic radiocarbon ages, linear sedimentation rate, coarse sand fraction, iceberg-rafted debris flux, biogenic silica flux, and biogenic silica concentrations. A sedimentary log (Armand et al., 2018) shows downcore variability in sedimentary features and composition. Variation in color on the sedimentary log represents sediment color logged onboard *RV Investigator* using the Munsell Color Chart. Four depth intervals, representing distinct changes in biogenic silica concentrations, are separated by gray lines. The horizontal dashed line corresponds with a marked decrease in the IBRD flux and an increase in biogenic silica concentrations. These changes are interpreted to represent the beginning of the deglacial transition between the last glacial period and the Holocene.

4.2. Detrital Mineralogy and Grain Morphology/Textures

The detrital mineralogy of KC14 consists of abundant quartz and feldspar with minor biotite and amphibole, and rare pyroxene and olivine. All detrital zircon grains in this study are smaller than 150 μm, with 72% falling within the fine fraction (<63 μm). Four fine zircon grains are located as inclusions within coarse detrital grains such as quartz, and as such are regarded as the coarse fraction for interpretation of transport processes. Of the zircons imaged under CL, 27% are fragmented predominantly across the prism axis of the grain (e.g., Figure 4: 3, 5, 6, 12, 15, 16, and 19) and 33% display multiple fine cracks (e.g., Figure 4: 5, 8, 9, 14, 15, 17, 18, 24, 25, and 26). All measured zircons ($n = 64$) are short and approximately equidimensional in shape, with aspect ratios between 1:1 and 2.15:1, although the fragmentation observed suggests many grains were originally more elongate prior to transport and deposition at the core site. Most of the grains imaged (80%) are angular to subangular with a minority displaying a subrounded morphology (Figure 4). Many of the zircons (53% of those imaged) reveal well-defined

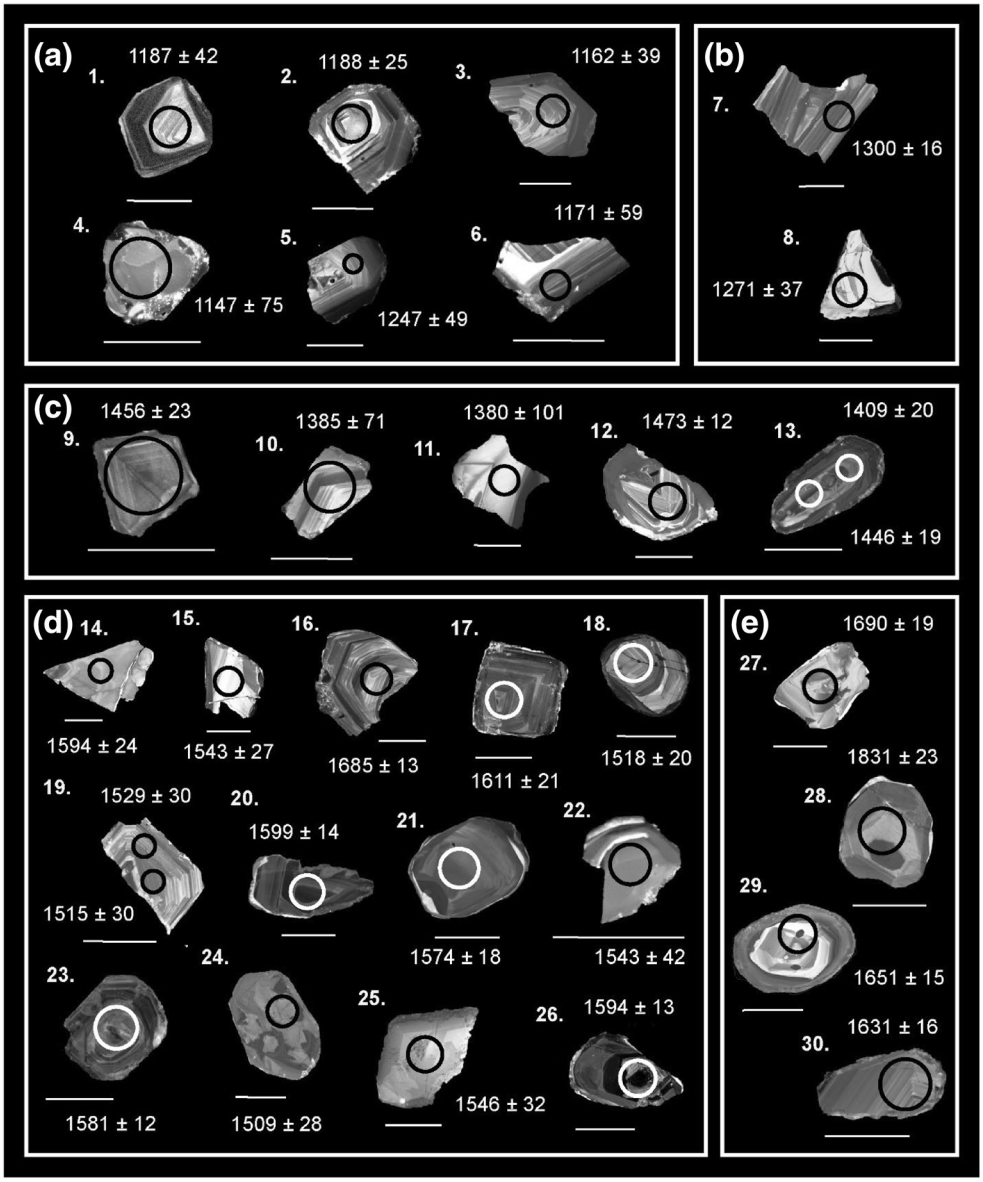

Figure 4. Representative cathodoluminescence images of detrital zircon grains from the intermediate fraction of KC14. Circles represent Laser Ablation-Inductively Coupled Plasma Mass Spectrometry analysis sites. Scale bars at 50 μm are shown as white lines under each grain. Ages are $^{207}Pb/^{206}Pb$ where > 1,000 Ma and ^{207}Pb-corrected $^{206}Pb/^{238}U$ where < 1,000 Ma ± 1σ error. Grains are divided into the following broad age groups, most of which are associated with major periods of magmatism and metamorphism in southern Australia and East Antarctica (Figure 2): (a) c. 1,250-1,100 Ma (Albany-Fraser/Wilkes Province Stage II, including the Moodini Supersuite) (b) c. 1,345-1,260 Ma (Albany-Fraser/Wilkes Province Stage I) (c) c. 1,480-1,390 Ma (Madura/Nuyina Province) (d) c. 1,610-1,490 Ma (Toolgana and Undawidgi supersuites of Coompana/Banzare Province) (e) > 1,610 Ma.

fine-scale oscillatory growth zoning, definitive of igneous zircon (e.g., Figure 4: 1–3, 5–7, 9, 10, 13, 16–20, 23, and 30) whereas others record a more complex growth history, with broader growth zones (e.g., Figure 4: 11), core-rim textures (e.g., Figure 4: 12, 13, 26, and 29), patchy and sector zoning (e.g., Figure 4: 4, 22, 24, 25, and 28) and localized recrystallization (e.g., Figure 4: 4, 12, and 23). A range of morphologies and textures are preserved in all age groups, dominated by short, commonly broken and angular grains with oscillatory zoning. Inspection of detrital apatite, titanite, and feldspar grains under a microscope similarly revealed dominantly angular and broken morphologies across all size fractions.

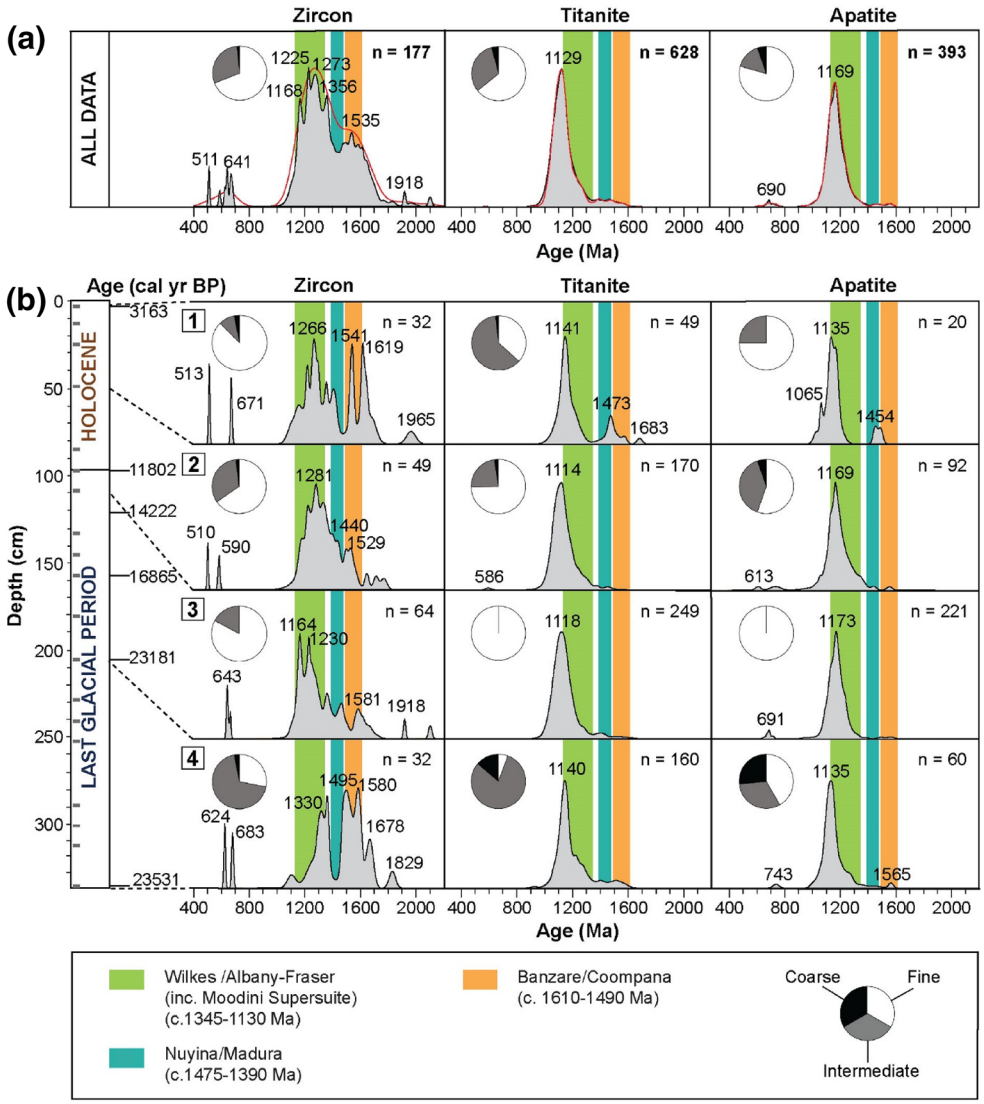

Figure 5. Detrital age signatures in KC14. (a) Age spectra for detrital zircon, titanite, and apatite for the entire KC14 core presented as probability-density plots (black curve, gray fill). Kernel density curve is shown in red. (b) Probability-density plots showing downcore age variability in detrital zircon, titanite, and apatite. Gray rectangles within the stylized core on left hand side show where sediment samples were taken from within each depth interval of KC14 for U-Pb analysis. Major age peaks and total number of analyses (*n*) are indicated. Age signatures of geological provinces in East Antarctica/southern Australia (as in Figure 2) are highlighted as colored bars for comparison. Although the Moodini Supersuite intrudes the Banzare/Coompana and Nuyina/Madura provinces, it is here grouped with the Wilkes Province/Albany-Fraser Orogen due to the overlap in age ranges. Pie charts show relative proportion of each mineral size fraction contributing to the age signature for each depth interval. Intervals 1–4 represent changes in biogenic silica concentration and are the same as those presented in Figure 3.

4.3. Detrital Zircon, Apatite, and Titanite Geochronology

Compiled U-Pb ages from all depth intervals of KC14 reveal dominant age populations between c. 1,360-1,100 Ma for detrital zircon and between c. 1,200-1,100 Ma for detrital titanite and apatite (Figure 5a). The detrital zircon age distribution exhibits strong multimodality; the dominant c. 1,360-1,100 Ma peaks representing 51% of the data set, with secondary peaks between c. 1,620-1,490 Ma (17%). A very small number of zircon analyses exhibit ages older than 1,620 Ma (8%) and between c. 700-500 Ma (5%). In contrast, the detrital titanite and apatite age distributions are largely unimodal, with most ages predominantly falling within the main c. 1,200-1,100 Ma population (66% and 86% for titanite and apatite respectively; Figure 5a).

A minor portion of detrital titanite and apatite analyses are older than c. 1,300 Ma and a very small population between c. 750 and 500 Ma is present in the detrital apatite record (Figure 5a).

Although the main c. 1,360-1,100 Ma age population is prevalent throughout the detrital zircon record, subtle changes in the relative proportions of age populations are observed with depth. Detrital zircon ages between c. 1,620 and 1,490 Ma are more prominent at the top and bottom of the core (intervals 1 and 4, Figure 5b). Major peaks within this population occur at c. 1,620 Ma and c. 1,540 Ma within interval 1 and at c. 1,580 Ma and c. 1,495 Ma within interval 4. In intervals 2 and 3, where biogenic silica is most abundant, detrital zircon grains within the c. 1,620-1,490 Ma age range are significantly reduced, and a minor c. 1,450-1,390 Ma population can be seen (Figure 5b) that is otherwise not discernible in the whole core record (Figure 5a). This population is also present as a small peak in interval 1 (at c. 1,400 Ma) but is completely absent from interval 4. The youngest age population (c. 750-500 Ma) exists in all depth intervals for detrital zircon and most of the apatite record (intervals 2–4, Figure 5b), but only exists within interval 2 for titanite (Figure 5b). These rare c. 750-500 Ma detrital zircon ($n = 9$), apatite ($n = 10$), and titanite ($n = 1$) grains were all obtained from the fine fraction. The detrital titanite and apatite age distributions are largely consistent throughout the transition from the glacial period through to the Holocene, with the addition of very minor peaks at c. 1,470 Ma and c. 1,450 Ma, respectively, in interval 1 of the core (Figure 5b).

4.4. Detrital Zircon, Apatite, and Titanite Trace Element Geochemistry

The detrital zircon grains in KC14 yield chondrite-normalized REE abundances between 10^{-4} and 10^{4} with steep heavy rare earth element (HREE) enrichment, a positive Ce anomaly and a negative Eu anomaly (Figure 6a), typical of magmatic zircon (e.g., Rubatto, 2017). A minority of grains exhibit flatter HREE signatures, more typical of high-temperature metamorphic zircon. The REE patterns in primary magmatic zircon (c. 1,150 Ma) from Chick Island basement rock samples (Maritati et al., 2019) span those of the detrital zircon in KC14 (Figure 6a). Detrital zircon Th/U ratios (Figure 6a inset) are variable but most have Th/U > 0.1, typical of magmatic zircon. Detrital apatite and titanite grains exhibit chondrite-normalized REE abundances between 10^{1} and 10^{5} and present a range of REE patterns (Figures S2a and S1b). However, most of these grains are LREE-enriched and present a strong negative Eu anomaly associated with a magmatic source rock composition (e.g., Belousova et al., 2002a; Olierook et al., 2019; O'Sullivan et al., 2020). A minor portion of detrital titanite grains reveal a positive Eu anomaly and HREE enrichment, associated with a metamorphic source rock type (Figure S2b). The detrital apatite and zircon geochemical data reveal a dominantly granitoid source rock type using discrimination plots from Belousova et al. (2002a, 2002b), respectively; Figures 6b,, and S2c). Most of the detrital titanite grains have high Fe concentrations ranging between 7,500 and 20,000 ppm, characteristic of igneous titanite (e.g., Olierook et al., 2019; Figure S2d).

4.5. Feldspar Pb-Isotopic Compositions

Feldspar analyzed from basement rocks from the Sabrina and Budd coasts (Figure 1) provide new potential source rock data sets to help assess offshore detrital provenance. Feldspar within a granite from Balaena Islets (PRR-21189) yield $^{206}Pb/^{204}Pb$ values of 16.6–16.7 and $^{207}Pb/^{204}Pb$ values of 15.5–15.6, plotting above the average crustal growth curve of Stacey and Kramers (1975; Figures 7a and 7b). In contrast, Chick Island basement feldspar grains from c. 1,150 Ma granodiorite (CI-814A2) and coeval granite xenoliths (CI-814B and CI-810A; Moodini Supersuite equivalents; Maritati et al., 2019) show a wider isotopic distribution with $^{206}Pb/^{204}Pb$ of 16.6–16.9 and $^{207}Pb/^{204}Pb$ of 15.4–15.6 (Figures 7a and 7b). Analyzed grains from both locations broadly overlap with Pb-isotopic signatures from other Australo-Antarctic domains (Mulder et al., 2019; Figure 7).

The Pb-isotopic compositions of feldspars in the offshore record are more diverse. Detrital K-feldspar and plagioclase from the coarse fraction in KC14 have $^{206}Pb/^{204}Pb$ of 15.9–17.5 and $^{207}Pb/^{204}Pb$ of 15.1–15.7 (Figure 7). These values predominantly span the mantle to average crust growth curves, with ~20% of the detrital feldspar compositions from KC14 overlapping the average-to-upper crustal basement rock compositions analyzed from the Balaena Islets (and Windmill Islands, defining the broader Wilkes Province) and Chick Island (near the boundary between the Nuyina and Banzare provinces; Figure 7).

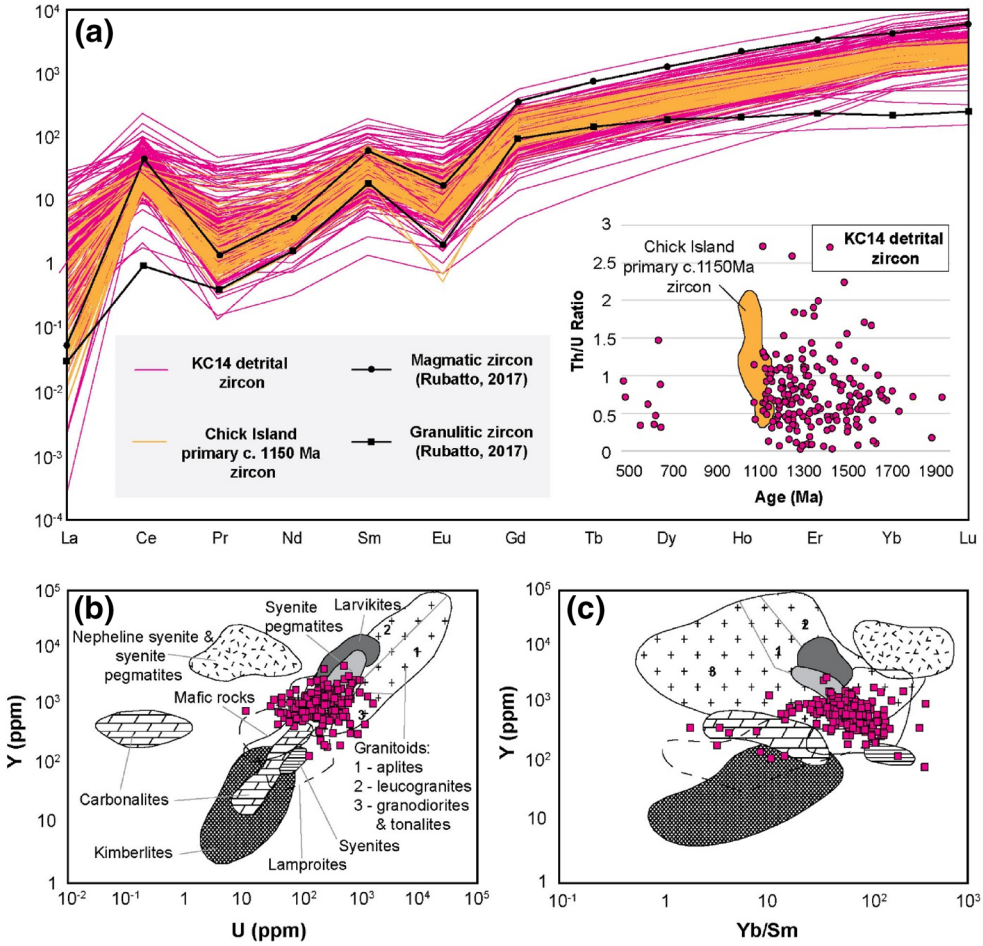

Figure 6. Detrital zircon trace element geochemistry. (a) Chondrite-normalized rare earth element (REE) diagrams and Th/U ratios for detrital zircon in KC14 and primary c. 1,150 Ma zircon from Chick Island basement rocks (Maritati et al., 2019). Typical REE compositions for magmatic and granulitic (i.e., high-temperature metamorphic) zircon from Rubatto (2017) are shown. (b, c) KC14 detrital zircon trace element data overlain on source rock discrimination diagrams from Belousova et al. (2002b).

5. Discussion

The rapidly retreating, fast-flowing Totten Glacier (Rignot et al., 2011; Figure 1b) is the closest major outlet glacier to the KC14 core site and is an obvious candidate for detrital delivery from the Totten glacial drainage basin. Indeed, the Totten Glacier is interpreted to have discharged sediment-laden meltwater and plumes throughout the Late Cenozoic, from the early development of the East Antarctic Ice Sheet to the present day (Donda et al., 2020), and is suggested to have contributed to the contourite ridge where KC14 was recovered (O'Brien et al., 2020).

The most recent interpretation of the subglacial geology in central Wilkes Land from Maritati et al. (2019) is based on matching geophysical signatures across the margins of southern Australia and East Antarctica and U-Pb analyses of primary and inherited zircon from rare plutonic outcrop at Chick Island. This tectonic framework suggests that the Wilkes, Nuyina, and Banzare provinces underlie the Totten catchment area, with the Totten Glacier exploiting a suture between the Wilkes and Nuyina provinces in the coastal region of the catchment, and the Banzare Province situated in the hinterland.

Based on these recent interpretations, it is anticipated that detritus on the continental slope and specifically sampled at KC14 should have an age and composition that reflects the Totten catchment basement terranes. In this paradigm, given that erosion is largely focused along the ice sheet margins at the coast (Golledge

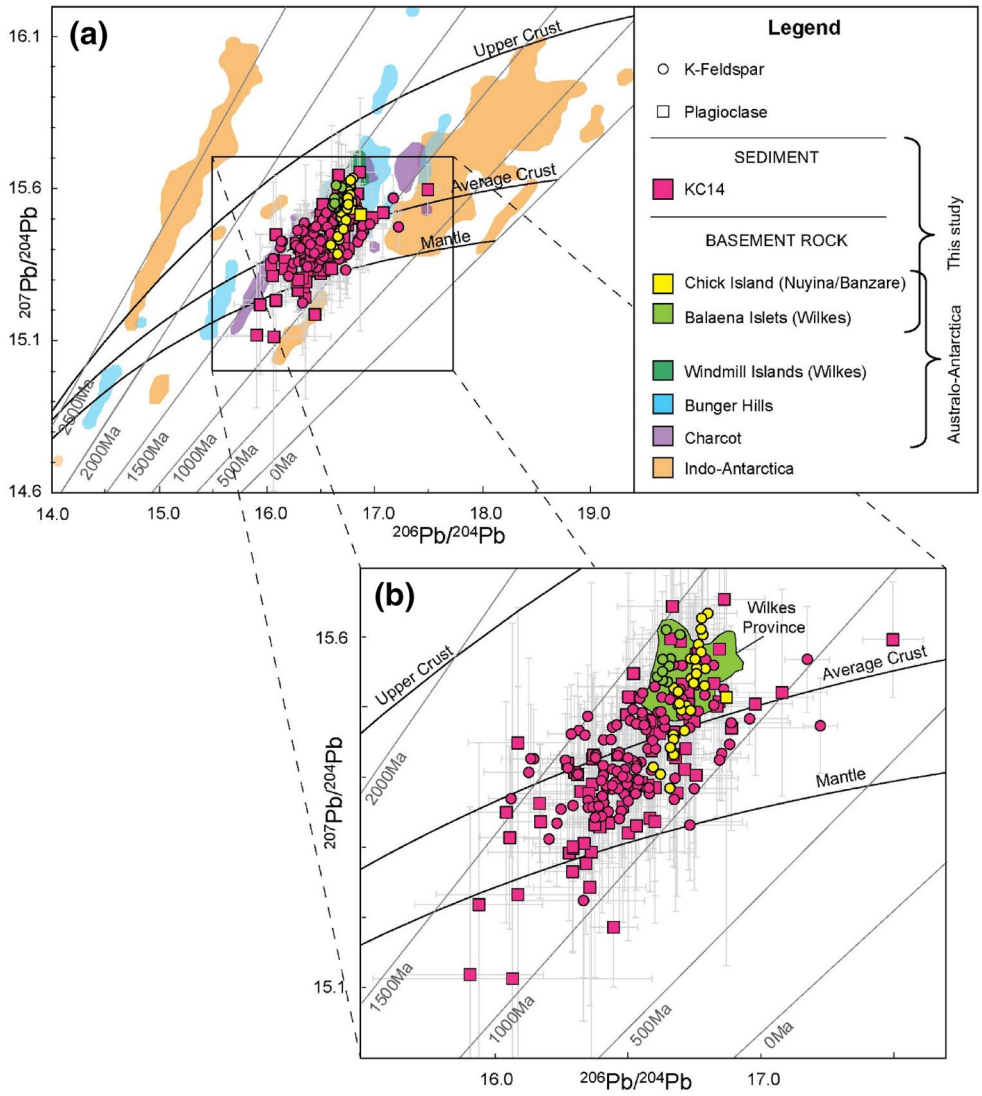

Figure 7. New detrital and bedrock feldspar Pb-isotopic data sets compared to regional Antarctic feldspar Pb-isotopic compositions. (a) Pb-isotopic signatures from detrital feldspar in KC14 (pink symbols) and basement rock feldspar from Balaena Islets (green symbols) and Chick Island (yellow symbols) overlain on Pb-isotopic feldspar domains from various locations in East Antarctica. Error bars (2σ) are shown for all analyses in this study. Indo-Antarctic basement rock data are from Flowerdew et al. (2013) and Mulder et al. (2019). Australo-Antarctic basement rock data are from Mulder et al. (2019) (Windmill Islands, Bunger Hills, Charcot) and this study (Chick Island and Balaena Islets). Growth curves for the mantle ($\mu = 9$), average crust ($\mu = 9.74$), and upper crust ($\mu = 12$) are plotted using the Pb isotope evolution model of Stacey and Kramers (1975). (b) Inset to (a), highlighting the analyses from this study. Black outline/green fill polygon shows Pb-isotopic compositions of basement rocks from the Wilkes Province (Windmill Islands and Balaena Islets).

et al., 2013; Jamieson et al., 2010), the source regions for detritus sampled at KC14 should be concentrated in the Wilkes and Nuyina provinces. We now explore this hypothesis in Section 5.1.

5.1. Was the Totten Glacier the Main Conduit for KC14 Detritus?

Previous work has identified that specific regions along the East Antarctic margin are characterized by distinct detrital zircon age signatures (Pierce et al, 2014), consistent with the known onshore geology (Veevers, 2012; Veevers & Saeed, 2011, and references therein). Three of these regions are defined here as Prydz Bay Sector (60°E–100°E), Wilkes Sector (100°E–136°E), and the Eastern Sector (136°E–180°E),

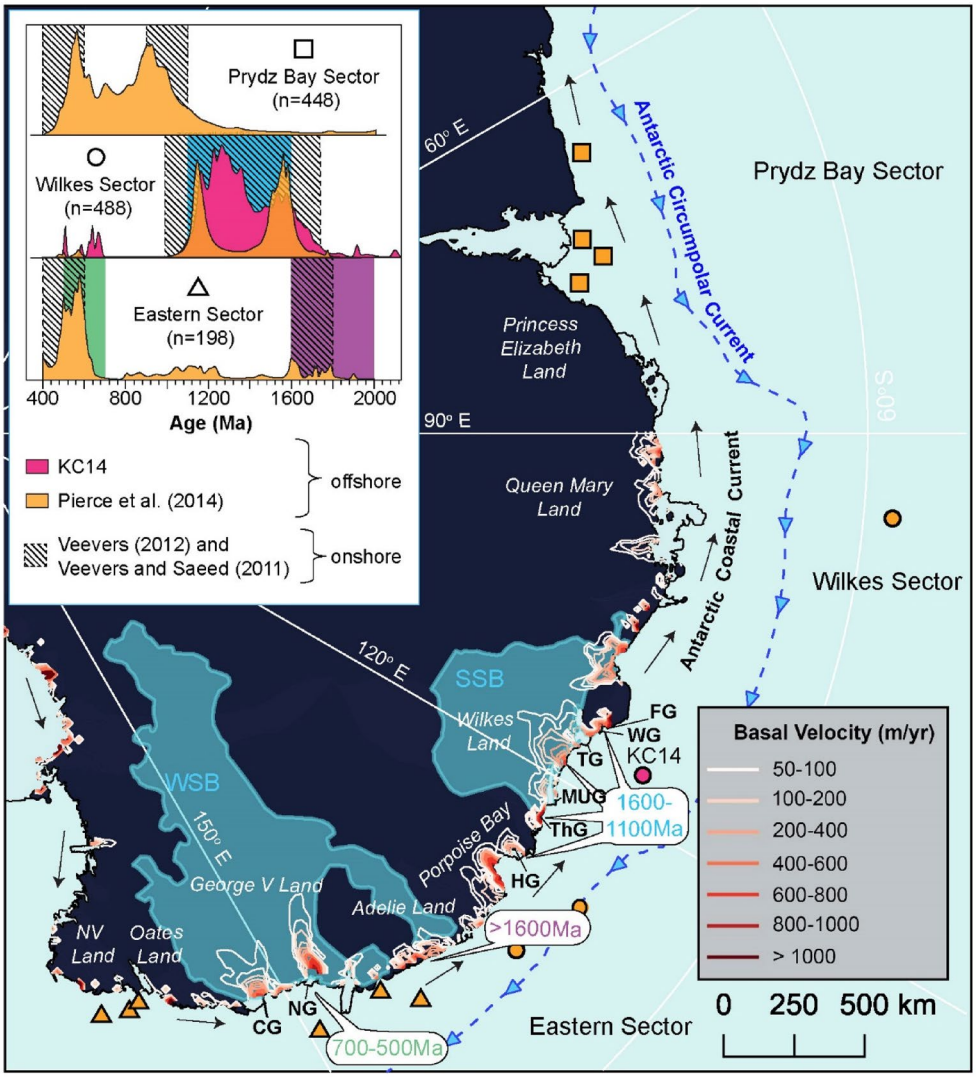

Figure 8. Comparison of predicted detrital source regions from the East Antarctic coast with onshore and offshore marine core records. Shown are locations of cores from Pierce et al. (2014) (orange symbols) and of KC14 (pink circle). Inset: U-Pb detrital zircon age signatures for each sector including KC14. Offshore data from Pierce et al. (2014). Striped boxes highlight dominant age populations of compiled onshore data from Veevers (2012) and Veevers and Saeed (2011). Colored bars represent main detrital age populations in KC14 and correspond with colored text on the map, indicating inferred provenance regions of each respective age population. CG, Cook Glacier; FG, Fox Glacier; HG, Holmes Glacier; MUG, Moscow University Glacier; NG, Ninnis Glacier; NV, Northern Victoria; SSB, Sabrina Sedimentary Basin (blue polygons); TG, Totten Glacier; ThG, Thompson Glacier; WG, Williamson Glacier; WSB, Wilkes Subglacial Basin. Blue-dashed line with arrows shows the position of the southern boundary of the eastward-flowing Antarctic Circumpolar Current (Orsi et al., 1995). Black arrows represent the westward-flowing Antarctic Coastal Current. Modeled basal velocity contours for an ice sheet slightly advanced relative to the present-day grounding line are from Aitken et al. (2016b) for the region between 90°E and 180°E.

broadly corresponding to those allocated by Pierce et al. (2014; Figure 8). Rocks of the Prydz Bay sector have peak zircon age populations at c. 990-900 Ma and c. 650-500 Ma (Veevers, 2012; Veevers & Saeed, 2011, and references therein). The Eastern Sector is dominated by Cambrian granites (c. 600-400 Ma) that intruded during the Ross Orogeny, with secondary older (>1,610 Ma) age peaks representative of Archean-Paleoproterozoic rocks of Adélie Land (Veevers, 2012; Veevers & Saeed, 2011, and references therein). The Wilkes Sector has a signature dominated by rocks that are predominantly Late Mesoproterozoic in age (c. 1,200-1,000 Ma). The detritus from KC14 has an age signature that is clearly distinct from the Prydz Bay and Eastern sectors (inset in Figure 8). Broadly, the detrital zircon age signature recorded at

KC14 matches well with other detrital sediment records from the Wilkes Sector further to the east (Pierce et al., 2014; Figure 8), but reveals additional prominent c. 1,360-1,220 Ma age peaks that are diagnostic of the Wilkes Province (Figures 5a and 8).

A derivation from the Totten Glacier catchment predicts mainly Wilkes and Nuyina-age signatures for KC14 detritus. The abundant c. 1,200-1,000 Ma zircon, apatite and titanite detritus in KC14 (Figure 5) could potentially be derived from voluminous plutonic rocks in any or all three of the proximal Wilkes, Nuyina, and Banzare provinces (Figure 2). Therefore, this age group is not particularly useful for identifying unique source regions in Wilkes Land. A minor proportion of c. 1,450-1,390 Ma zircon, c. 1,470 Ma titanite, and c. 1,450 Ma apatite in KC14 suggests some of the detritus was likely sourced from the Nuyina Province (c. 1,475-1,390 Ma). However, a significant component of detrital zircon with an age between c. 1,620-1,490 Ma is also present in KC14 (Figure 5), characteristic of the c. 1,610 Ma Toolgana and c. 1,490 Ma Undawidgi supersuites in the Banzare Province. This c. 1,620-1,490 Ma Banzare signature, coupled with the distinctive c. 1,360-1,220 Ma Wilkes signature, implicates both these provinces as dominant sources. The Pb-isotopic compositions of KC14 detrital feldspar grains partially overlap feldspar compositions from plutonic rocks in the Balaena Islets (Wilkes Province) and Chick Island (near the boundary of Nuyina and Banzare provinces), supporting this interpretation (Figure 7).

There are a number of scenarios that could explain the scarcity of Nuyina-age detritus (which is a signature expected if the Totten Glacier was the main conduit) in addition to the abundance of Banzare-age detritus at the KC14 core site. One scenario is that some erosion was focused in the hinterland of the Totten catchment, encapsulating Banzare crust. However, much of this region is covered by kilometers of Sabrina Basin sedimentary strata (Aitken et al., 2016b) so we do not expect crystalline bedrock exposure. Furthermore, the high angularity and broken morphologies of most detrital grains from all size fractions in KC14 (Figure 4) supports a relatively local provenance and argues against recycling through preglacial sedimentary systems. This is further supported by the high abundance of detrital feldspar grains which are typically unable to withstand prolonged weathering and erosion (Johnson et al., 2018).

A second scenario could be envisaged whereby the Nuyina Province may be less extensive than interpreted by Maritati et al. (2019), such that basal erosion in the coastal region of the Totten catchment sources Banzare crust in addition to Wilkes. This interpretation could account for the strong Banzare-age signature and weak Nuyina-age signature in the detrital zircon record (Figure 5a). Testing of this hypothesis is difficult without higher-resolution geophysical data linking the conjugate margins of southern Australia and East Antarctica and/or geological sampling (e.g., dredging of basement rock ridges or sampling of proximal marine sediment cores).

A third scenario that could explain the scarcity of Nuyina-age detritus is an underrepresentation of mafic rock types in the detrital zircon record (Licht & Hemming, 2017; Shao et al., 2019). The Nuyina Province likely comprises juvenile mafic rocks similar to the Arubiddy Ophiolite Complex of the Madura Province (Figure 2b). Although detailed analysis of zircon grains revealed well-developed oscillatory growth zoning (Figure 4) and trace element signatures typical of a felsic igneous source (Figures 6 and S2), this could be a biased record related to the high abundance of zircon in felsic rocks compared to the typically small amounts of zircon contained in mafic rocks (Licht & Hemming, 2017; Shao et al., 2019). Another bias in favor of felsic rock compositions may also be introduced by the different weathering rates of mafic and felsic rock types. Mafic rocks have a lower resistance to weathering, leading to limited preservation of mafic rock components over time (Licht & Hemming, 2017). Derivation of KC14 detritus from at least some mafic-intermediate crust is supported by the presence of minor amphibole, pyroxene, and olivine grains. Evidence for mafic source components is also provided by the spread in detrital feldspar Pb-isotopic compositions (plagioclase in particular) to mantle-like values (Figure 7). This signature suggests the presence of unexposed juvenile rocks in the hinterland, likely within the Nuyina and Banzare provinces, related to reworking of oceanic crust during a series of accretionary tectonic events (Kirkland et al., 2017; Maritati et al., 2019; Spaggiari et al., 2018).

Although the underrepresentation of mafic source rocks in the detrital zircon record potentially explains the paucity of Nuyina-age detritus in KC14, this scenario alone does not explain the abundance of Banzare-age detritus. A fourth scenario, and one that we suggest is most plausible, is that the Totten Glacier was one of a number of outlet glaciers that contributed detritus to KC14, as described in Section 5.2 below.

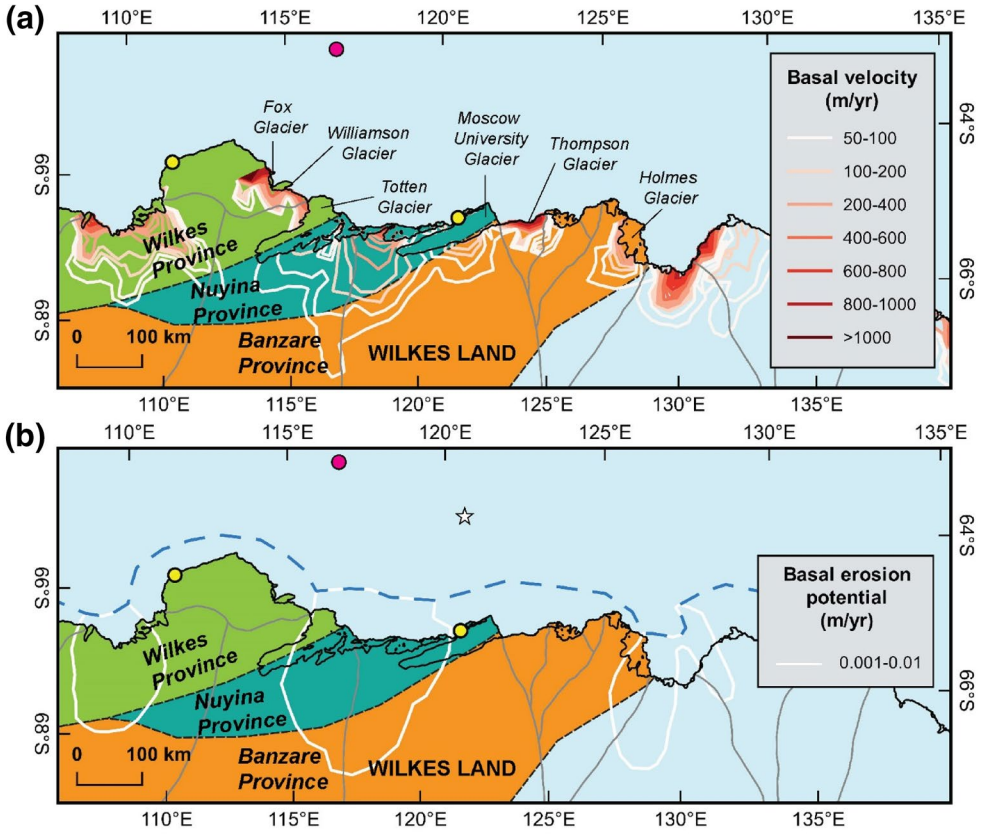

Figure 9. Basal ice sheet velocity in central Wilkes Land overlain on subglacial geological provinces interpreted from geophysical data and coastal outcrop (Aitken et al., 2014; Maritati et al., 2019). Coastal (yellow) and offshore (pink) sample locations are shown. Gray lines mark the boundaries of ice drainage basins (Mouginot et al., 2017). (a) Map showing modeled ice sheet basal velocity contours predicted for an ice sheet slightly advanced relative to the present from Aitken et al. (2016b) and clipped to the modern grounding line (Mouginot et al., 2017). (b) Map showing modeled basal erosion potential at 21 ka from Golledge et al. (2013). The modeled maximum extent of the ice sheet is indicated with a blue dashed line (Golledge et al., 2013). The position of a grounding zone wedge (GSW) identified by Post et al. (2020) is shown (white star), as new evidence indicating the former maximum extent of the ice sheet at that location.

5.2. A Case for a Distributed Wilkes Land Provenance for KC14

Two main age distribution patterns are observed in the detrital zircon record. In intervals 1 and 4 of KC14 (broadly equivalent to the Holocene and last glacial period, respectively), detrital zircon age peaks associated with the Banzare Province (c. 1,620-1,490 Ma) are prevalent alongside the c. 1,360-1,100 Ma Wilkes signature (Figure 5b). In the middle biosiliceous portion of the core (intervals 2 and 3, Figure 5b), Banzare-age peaks are reduced and Nuyina-age peaks (c. 1,450-1,390 Ma) are more prominent. We suggest these subtle changes in the detrital zircon record over time support the supply of detritus from multiple source regions. Below, we relate downcore changes in sediment provenance to temporal changes in the climate and ice sheet configuration.

5.2.1. A Broad Source Region During Interglacials

The most recently deposited sediment is captured by KC14 interval 1 (Figure 5b), which should therefore yield an age signature that is most representative of the subglacial rock types being eroded at the base of the ice sheet in the present day. The Banzare-age detrital zircon signature in this interval suggests that some of this more recently deposited detritus was sourced from where the Banzare Province is exposed to the base of the ice sheet at or close to the coast. The interpreted extension of the Banzare Province beneath multiple subglacial catchments east of the Totten catchment (Maritati et al., 2019) suggests likely detrital contri-

butions from the Moscow University, Thompson, and Holmes glaciers (Figure 9). This idea is supported by recent interpretations of the continental slope morphology that suggest that the contourite ridge from which KC14 was recovered is fed not only by detritus from the Totten Glacier, but also by fine sediment plumes transported westward across the slope by the Antarctic Coastal Current (O'Brien et al., 2020). With an ice sheet slightly advanced relative to modern grounding line, the ice sheet model of Aitken et al. (2016b) predicts high basal erosion (using basal velocity as a proxy) across a broad coastal area of central Wilkes Land (Figure 9a). The dominance of Wilkes and Banzare-age peaks in interval 1 of our marine core record supports the predictions of this ice sheet model which shows high basal erosion focused in zones mostly underlain by the Wilkes and Banzare provinces (Figures 5b and 9a).

5.2.2. Debris Flows During the Last Glacial Period

Curiously, the detrital zircon signature during the glacial (interval 4) resembles that of the current interglacial (interval 1) described above (Figure 5b). We interpret the detrital age signal in the glacial section of KC14 (interval 4; Figures 3 and 5) to represent reworked sediment remobilized off the shelf and deposited downslope during glacial advance, a process recently inferred in this region (O'Brien et al., 2020; Post et al., 2020) and in previous studies around the Antarctic margin (e.g., Diekmann et al., 2000; Dowdeswell et al., 2006, 2004; Gales et al., 2013; Pudsey, 2000). This interpretation is supported by the high glacial sedimentation rate (377 cm/Kyr; interval 4, Figure 3), at a time when basal erosion by the ice sheet was minimum (Golledge et al., 2013; Figure 9b), suggesting that reworking of shelf sediments by debris flows was the most likely process contributing to the high sediment accumulation (O'Brien et al., 2020; Post et al., 2020). The relatively small concentrations of biogenic silica measured in the glacial section of the core (interval 4%; 1.9%–7.9%) likely comprise reworked diatoms from earlier warm periods that were redeposited with the sediment from the continental shelf, explaining the high biogenic silica flux during this same glacial period (interval 4, Figure 3). Coarse debris (250 μm–2 mm) that matches the criteria of IBRD was likely mobilized by downslope sediment transport. This process explains the higher calculated "IBRD" flux during the glacial (Figure 3), when iceberg calving would have been infrequent and the quantity of IBRD is expected to be low (Bertram et al., 2018; Wilson et al., 2018). A mixture of this coarse debris and fallout of finer sediment from suspension in sediment-laden plumes likely contributed to the maintenance of the large contourite ridge where KC14 is located (O'Brien et al., 2020; Post et al., 2020). The similarity in age distribution between intervals 1 and 4 suggests that the sediment reworked in debris flows as the ice sheet advanced was initially deposited during past warmer climate periods, when the position of the retreated ice sheet margin and the provenance of continentally derived detritus was similar to that of the present day.

5.2.3. A Proximal Provenance During Deglaciation

A prominent decline in the sedimentation rate from 377 cm/Kyr to 8 cm/Kyr at c. 23.2 cal years BP (Figure 3) indicates the ceasing of abundant sediment supply in debris flows to the slope. We interpret this decrease in sedimentation as the point when the ice sheet reached its maximum extent, and the associated reworking of shelf sediments ceased. The onset of deglaciation (c. 16.9-14.2 cal years BP) is marked by a rise in biogenic silica concentrations representing a growth in primary productivity and warmer, ice-free conditions above the core site (intervals 2 and 3, Figure 3). During this time, the sedimentation rate increased to 14 cm/Kyr and IBRD became more abundant, reflecting a change in the mode of sediment transport to the continental slope. While sedimentation during the glacial period was dominated by the supply of reworked sediment in mass flows, deglacial sedimentation was likely controlled by the release of englacial IBRD in sediment-laden meltwater fluxes associated with climate warming and ice sheet retreat, as interpreted in other studies in East Antarctica (e.g., Bertram et al., 2018; Wilson et al., 2018).

The deglacial sediment provenance signature is represented by detrital ages from biosiliceous sediments in intervals 2 and 3 of the core (Figures 3 and 5b). In comparison to intervals 1 and 4, the more prominent Wilkes and Nuyina-age signatures, coupled with a significantly reduced Banzare-age signal in these deglacial intervals, suggests that detritus was sourced from the coastal region of the Totten catchment area. At the onset of deglaciation, with an ice sheet extended further offshore of its present-day posi-

tion, the terminus of the Totten Glacier was situated in closer proximity to the KC14 core site and would likely be the principal outlet for detritus during this time. Recently, Prothro et al. (2018) interpreted that most englacial debris that melted out of the base of ice shelves in the Ross Sea region during retreat was deposited proximal to the grounding line. We interpret this to be the case in central Wilkes Land. With a narrower "cone of influence," the abundant detritus being supplied by the Totten Glacier to the slope would dampen the signal produced from detritus from more distal sources, explaining the relatively enhanced Nuyina-age signature and reduced Banzare-age signature in the detrital zircon record (intervals 2 and 3, Figure 5b).

5.2.4. Evidence for Minor Far-Field Provenance

Minor detrital c. 750-500 Ma ages are present throughout the detrital zircon record, that are not known to be characteristic of basement rocks of central Wilkes Land nor the conjugate regions in southern Australia. The compiled age spectra from the offshore (Pierce et al., 2014) and onshore (Veevers, 2012; Veevers & Saeed, 2011) records of the Eastern Sector show a dominant age population between c. 740-400 Ma (Figure 8). Westward transport of detritus over long distances from one sector to another by icebergs driven by the Antarctic Coastal Current is supported by evidence from warm climates and transitions of the Early Pliocene (Cook et al., 2014; Williams et al., 2010). Icebergs calved off from the Eastern Sector have been observed tracking westward along the shelf to the Wilkes Sector (Budge & Long, 2018). We propose westward transport of a minor component of detritus from the Eastern Sector via icebergs driven by the Antarctic Coastal Current to the KC14 core site. This hypothesis would account for the rare, but distinct c. 750-500 Ma detrital age population characteristic of the basement rock and intruded granites of George V Land (e.g., Lamarque et al., 2018). Provenance from the east could also account for minor older c. 2,200-1,700 Ma detrital zircon ages that correlate with Archean and Paleoproterozoic rocks of the Adélie Land coast (e.g., Ménot et al., 2007; Figure 8).

6. Conclusions

This investigation presents the first sediment provenance record from the continental slope of central Wilkes Land, defining the sedimentary environment, transport, and source of detritus to this part of the Wilkes Sector from c. 23.5 ka to present. Detailed multiproxy analyses allow the following conclusions to be drawn:

1. The main Mesoproterozoic (c. 1,360-1,000 Ma and c. 1,620-1,490 Ma) age populations in the KC14 detritus indicate sourcing from dominantly felsic granitoid rocks of the proximal Wilkes and Banzare provinces, with smaller contributions from the adjacent Nuyina Province (c. 1,450-1,390 Ma) in central Wilkes Land. The unexpectedly small contribution from Nuyina Province, and relative importance of material from the Banzare Province, is hypothesized to reflect sourcing of detritus from a broad source region, including the Totten Glacier catchment and subglacial catchments further east.
2. Debris flows instigated by the advancing ice sheet remobilized sediments from the continental shelf and redeposited them on the slope during the last glacial period. These sediments, deposited prior to glacial advance, have the same provenance signature as detritus deposited during the current interglacial.
3. The deglacial signature is dominated by detritus from the Wilkes and Nuyina provinces that underlie Totten Glacier, suggesting dominant sourcing of detritus from the coastal region of the Totten catchment area when the ice sheet margin was extended further offshore of its present-day position. This is likely due to the proximity of Totten Glacier to the core site and the dampening of detrital age signatures from more distal source regions during this time
4. Minor c. 750-500 Ma and 2,200-1,700 Ma detrital zircon in KC14 was likely derived from rocks in the Eastern Sector and transported to the core site via icebergs driven by the Antarctic Coastal Current

This new sediment provenance record provides the first offshore evidence from the Sabrina Coast to support existing subglacial bedrock interpretations from available geophysical and rare outcrop geological data in central Wilkes Land. These findings can be used to support plate tectonic reconstructions and to help infer the properties of the Antarctic crust that are relevant to basal ice sheet conditions and associated ice sheet configuration.

Data Availability Statement

Data archived with Pangaea are referenced in this article and can be accessed online using the following link: https://doi.pangaea.de/10.1594/PANGAEA.907799

Acknowledgments
We acknowledge the Marine National Facility, the IN2017-V01 scientific party led by the Chief Scientists L. K. Armand and P. O'Brien, MNF support staff and ASP crew members led by Capt. M. Watson for sample recovery, primary data collection and support and assistance onboard the *RV Investigator*. We thank S. Meffre and J. Thompson (Earth Sciences/CODES, University of Tasmania), S. Feig and K. Goemann (Central Science Laboratory, University of Tasmania) and Nils Jansen (Institute for Marine and Antarctic Studies, University of Tasmania) for their expertise and technical assistance and A. Maritati for Pb-Pb analysis of the basement rock feldspars used in this study. We also thank the reviewers and editors for their constructive comments and suggestions on previous versions of this article. Sian Tooze was supported by a PhD scholarship from the Australian Research Council's Special Research Initiative for the Antarctic Gateway Partnership (Project ID SR140300001). Taryn L. Noble acknowledges support from the Science and Industry Endowment Fund, and Australian Antarctic Science Program Grant 4419. This research used samples (from Balaena Islets) provided by the Polar Rock Repository (PRR). The PRR is sponsored by the National Science Foundation Office of Polar Programs. All data to support our conclusions can be found in this article, in the supporting information and archived with Pangaea database.

References

Aitken, A. R. A., Betts, P. G., Young, D. A., Blankenship, D. D., Roberts, J. L., & Siegert, M. J. (2016a). The Australo-Antarctic Columbia to Gondwana transition. *Gondwana Research*, *29*(1), 136–152. https://doi.org/10.1016/j.gr.2014.10.019

Aitken, A. R. A., Roberts, J. L., Van Ommen, T. D., Young, D. A., Golledge, N. R., Greenbaum, J. S., et al. (2016b). Repeated large-scale retreat and advance of Totten Glacier indicated by inland bed erosion. *Nature*, *533*, 385–389. https://doi.org/10.1038/nature17447

Aitken, A. R. A., Young, D. A., Ferraccioli, F., Betts, P. G., Greenbaum, J. S., Richter, T. G., et al. (2014). The subglacial geology of Wilkes Land, East Antarctica. *Geophysical Research Letters*, *41*(7), 2390–2400. https://doi.org/10.1002/2014GL059405

Amblas, D., & Canals, M. (2016). Contourite drifts and canyon-channel systems on the Northern Antarctic Peninsula Pacific margin. *Geological Society Memoir*, *46*(1), 393–394. https://doi.org/10.1144/M46.17

Armand, L. K., O'Brien, P. E., & On-board Scientific Party. (2018). *Interactions of the Totten Glacier with the Southern Ocean through multiple glacial cycles (IN2017-V01): Post-survey report.* Canberra, ACT: Research School of Earth Sciences, Australian National University. https://doi.org/10.4225/13/5acea64c48693

Baker, J., Peate, D., Waight, T., & Meyzen, C. (2004). Pb isotopic analysis of standards and samples using a 207Pb-204Pb double spike and thallium to correct for mass bias with a double-focusing MC-ICP-MS. *Chemical Geology*, *211*(3–4), 275–303. https://doi.org/10.1016/j.chemgeo.2004.06.030

Barfod, G. H., Krogstad, E. J., Frei, R., & Albarède, F. (2005). Lu-Hf and PbSL geochronology of apatites from proterozoic terranes: A first look at Lu-Hf isotopic closure in metamorphic apatite. *Geochimica et Cosmochimica Acta*, *69*(7), 1847–1859. https://doi.org/10.1016/j.gca.2004.09.014

Belousova, E. A., Griffin, W. L., O'Reilly, S. Y., & Fisher, N. I. (2002a). Apatite as an indicator mineral for mineral exploration: Trace-element compositions and their relationship to host rock type. *Journal of Geochemical Exploration*, *76*(1), 45–69. https://doi.org/10.1016/S0375-6742(02)00204-2

Belousova, E. A., Griffin, W. L., O'Reilly, S. Y., & Fisher, N. I. (2002b). Igneous zircon: Trace element composition as an indicator of source rock type. *Contributions to Mineralogy and Petrology*, *143*(5), 602–622. https://doi.org/10.1007/s00410-002-0364-7

Berry, R., Thompson, J., Meffre, S., & Goemann, K. (2016). U–Th–Pb monazite dating and the timing of arc–continent collision in East Timor. *Australian Journal of Earth Sciences*, *63*(4), 367–377. https://doi.org/10.1080/08120099.2016.1217930

Bertram, R. A., Wilson, D. J., van de Flierdt, T., McKay, R. M., Patterson, M. O., Jimenez-Espejo, F. J., et al. (2018). Pliocene deglacial event timelines and the biogeochemical response offshore Wilkes Subglacial Basin, East Antarctica. *Earth and Planetary Science Letters*, *494*, 109–116. https://doi.org/10.1016/j.epsl.2018.04.054

Black, L. P., Kamo, S. L., Allen, C. M., Aleinikoff, J. N., Davis, D. W., Korsch, R. J., & Foudoulis, C. (2003). TEMORA 1: A new zircon standard for phanerozoic U-Pb geochronology. *Chemical Geology*, *200*(1–2), 155–170. https://doi.org/10.1016/S0009-2541(03)00165-7

Boger, S. D. (2011). Antarctica—Before and after Gondwana. *Gondwana Research*, *19*(2), 335–371. https://doi.org/10.1016/j.gr.2010.09.003

Budge, J. S., & Long, D. G. (2018). A comprehensive database for antarctic iceberg tracking using scatterometer data. *IEEE Journal of Selected Topics in Applied Earth Observations and Remote Sensing*, *11*(2), 434–442. https://doi.org/10.1109/JSTARS.2017.2784186

Cameron, R. L., Loken, O. H., & Molholm, J. R. T. (1958). *USNC-IGY Antarctic glaciological data. Field work 1957 and 1958. Part 1.* Columbus, OH: Ohio State University Research Foundation Report. Retrieved from http://hdl.handle.net/1811/33913

Chew, D. M., Sylvester, P. J., & Tubrett, M. N. (2011). U-Pb and Th-Pb dating of apatite by LA-ICPMS. *Chemical Geology*, *280*(1–2), 200–216. https://doi.org/10.1016/j.chemgeo.2010.11.010

Clark, D. J., Hensen, B. J., & Kinny, P. D. (2000). Geochronological constraints for a two-stage history of the Albany-Fraser Orogen, Western Australia. *Precambrian Research*, *102*(3–4), 155–183. https://doi.org/10.1016/S0301-9268(00)00063-2

Cook, C. P., Hill, D. J., van de Flierdt, T., Williams, T., Hemming, S. R., Dolan, A. M., et al. (2014). Sea surface temperature control on the distribution of far-traveled Southern Ocean ice-rafted detritus during the Pliocene. *Paleoceanography*, *29*(6), 533–548. https://doi.org/10.1002/2014PA002625

Coulson, I. M., Villeneuve, M. E., Dipple, G. M., Duncan, R. A., Russell, J. K., & Mortensen, J. K. (2002). Time-scales of assembly and thermal history of a composite felsic pluton: Constraints from the Emerald Lake area, northern Canadian Cordillera, Yukon. *Journal of Volcanology and Geothermal Research*, *114*(3–4), 331–356. https://doi.org/10.1016/S0377-0273(01)00294-3

De Santis, L., Brancolini, G., Accettella, D., Cova, A., Caburlotto, A., Donda, F., et al. (2007). New insights into submarine geomorphology and depositional processes along the George V Land continental slope and upper rise (East Antarctica). In A. K. Cooper, C. R. Raymond, et al. (Eds.), *Keystone in a Changing World-Online Proceedings of the 10th International Symposium on Antarctic Earth Sciences* (Vol. 1047, pp. 1–5). Reston, VA: USGS open-file report 2007-1047, extended abstract 061. United States Geological Survey.

DeMaster, D. J. (1981). The supply and accumulation of silica in the marine environment. *Geochimica et Cosmochimica Acta*, *45*(10), 1715–1732. https://doi.org/10.1016/0016-7037(81)90006-5

Diamond, D. (2002). Determination of silicate in brackish or seawater by flow injection analysis. QuickChem Method 31-114-27-1-D. *Lachat Instruments QuickChem Method Manual*.

Diekmann, B., Kuhn, G., Rachold, V., Abelmann, A., Brathauer, U., Fütterer, D. K., et al. (2000). Terrigenous sediment supply in the Scotia Sea (Southern Ocean): Response to late quaternary ice dynamics in Patagonia and on the Antarctic Peninsula. *Palaeogeography, Palaeoclimatology, Palaeoecology*, *162*(3–4), 357–387. https://doi.org/10.1016/S0031-0182(00)00138-3

Donda, F., Brancolini, G., O'Brien, P. E., De Santis, L., & Escutia, C. (2007). Sedimentary processes in the Wilkes Land margin: A record of the cenozoic East Antarctic ice sheet evolution. *Journal of the Geological Society*, *164*(1), 243–256. https://doi.org/10.1144/0016-76492004-159

Donda, F., Leitchenkov, G., Brancolini, G., Romeo, R., De Santis, L., Escutia, C., et al. (2020). The influence of Totten Glacier on the Late Cenozoic sedimentary record. *Antarctic Science*, *32*(4), 288–300. https://doi.org/10.1017/S0954102020000188

Dowdeswell, J. A., Evans, J., O'Cofaigh, C., & Anderson, J. B. (2006). Morphology and sedimentary processes on the continental slope off Pine Island Bay, Amundsen Sea, West Antarctica. *Bulletin of the Geological Society of America*, *118*(5–6), 606–619. https://doi.org/10.1130/B25791.1

Dowdeswell, J. A., Ó Cofaigh, C., & Pudsey, C. J. (2004). Continental slope morphology and sedimentary processes at the mouth of an Antarctic palaeo-ice stream. *Marine Geology*, *204*(1–2), 203–214. https://doi.org/10.1016/S0025-3227(03)00338-4

Fernandez, R., Gulick, S., Domack, E., Montelli, A., Leventer, A., Shevenell, A., & Frederick, B. (2018). Past ice stream and ice sheet changes on the continental shelf off the Sabrina Coast, East Antarctica. *Geomorphology*, *317*, 10–22. https://doi.org/10.1016/j.geomorph.2018.05.020

Fitzsimons, I. C. W. (2003). Proterozoic basement provinces of southern and southwestern Australia, and their correlation with Antarctica. *Geological Society—Special Publications*, *206*(1), 93–130. https://doi.org/10.1144/GSL.SP.2003.206.01.07

Flowerdew, M. J., Tyrrell, S., Boger, S. D., Fitzsimons, I. C. W., Harley, S. L., Mikhalsky, E. V., & Vaughan, A. P. M. (2013). Pb isotopic domains from the Indian Ocean sector of Antarctica: Implications for past Antarctica-India connections. *Geological Society—Special Publications*, *383*(1), 59–72. https://doi.org/10.1144/SP383.3

Fretwell, P., Pritchard, H. D., Vaughan, D. G., Bamber, J. L., Barrand, N. E., Bell, R., et al. (2013). Bedmap2: Improved ice bed, surface and thickness datasets for Antarctica. *The Cryosphere*, *7*(1), 375–393. https://doi.org/10.5194/tc-7-375-2013

Gales, J. A., Larter, R. D., Mitchell, N. C., & Dowdeswell, J. A. (2013). Geomorphic signature of Antarctic submarine gullies: Implications for continental slope processes. *Marine Geology*, *337*, 112–124. https://doi.org/10.1016/j.margeo.2013.02.003

Golledge, N. R., Levy, R. H., McKay, R. M., Fogwill, C. J., White, D. A., Graham, A. G. C., et al. (2013). Glaciology and geological signature of the last glacial maximum Antarctic ice sheet. *Quaternary Science Reviews*, *78*, 225–247. https://doi.org/10.1016/j.quascirev.2013.08.011

Greenbaum, J. S., Blankenship, D. D., Young, D. A., Richter, T. G., Roberts, J. L., Aitken, A. R. A., et al. (2015). Ocean access to a cavity beneath Totten Glacier in East Antarctica. *Nature Geoscience*, *8*(4), 294–298. https://doi.org/10.1038/ngeo2388

Gulick, S. P. S., Shevenell, A. E., Montelli, A., Fernandez, R., Smith, C., Warny, S., et al. (2017). Initiation and long-term instability of the east Antarctic ice sheet. *Nature*, *552*(7684), 225–229. https://doi.org/10.1038/nature25026

Halpin, J. A., Jensen, T., McGoldrick, P., Meffre, S., Berry, R. F., Everard, J. L., et al. (2014). Authigenic monazite and detrital zircon dating from the Proterozoic Rocky Cape Group, Tasmania: Links to the Belt-Purcell Supergroup, North America. *Precambrian Research*, *250*, 50–67. https://doi.org/10.1016/j.precamres.2014.05.025

Hawke, M. L., Meffre, S., Stein, H., Hilliard, P., Large, R., & Gemmell, J. B. (2015). Geochronology of the DeGrussa volcanic-hosted massive sulphide deposit and associated mineralisation of the Yerrida, Bryah and Padbury Basins, Western Australia. *Precambrian Research*, *267*, 250–284. https://doi.org/10.1016/j.precamres.2015.06.011

Horstwood, M. S. A., Košler, J., Gehrels, G., Jackson, S. E., McLean, N. M., Paton, C., et al. (2016). Community-derived standards for LA-ICP-MS U-(Th-)Pb geochronology—Uncertainty propagation, age interpretation and data reporting. *Geostandards and Geoanalytical Research*, *40*(3), 311–332. https://doi.org/10.1111/j.1751-908X.2016.00379.x

Jamieson, S. S. R., Sugden, D. E., & Hulton, N. R. J. (2010). The evolution of the subglacial landscape of Antarctica. *Earth and Planetary Science Letters*, *293*(1–2), 1–27. https://doi.org/10.1016/j.epsl.2010.02.012

Jochum, K. P., Weis, U., Schwager, B., Stoll, B., Wilson, S. A., Haug, G. H., et al. (2016). Reference values following ISO guidelines for frequently requested rock reference materials. *Geostandards and Geoanalytical Research*, *40*(3), 333–350. https://doi.org/10.1111/j.1751-908X.2015.00392.x

Jochum, K. P., Wilson, S. A., Abouchami, W., Amini, M., Chmeleff, J., Eisenhauer, A., et al. (2011). GSD-1G and MPI-DING reference glasses for in situ and bulk isotopic determination. *Geostandards and Geoanalytical Research*, *35*(2), 193–226. https://doi.org/10.1111/j.1751-908X.2010.00114.x

Johnson, S. P., Kirkland, C. L., Evans, N. J., McDonald, B. J., & Cutten, H. N. (2018). The complexity of sediment recycling as revealed by common Pb isotopes in K-feldspar. *Geoscience Frontiers*, *9*(5), 1515–1527. https://doi.org/10.1016/j.gsf.2018.03.009

Kirkland, C. L., Smithies, R. H., Spaggiari, C. V., Wingate, M. T. D., Quentin de Gromard, R., Clark, C., et al. (2017). Proterozoic crustal evolution of the Eucla basement, Australia: Implications for destruction of oceanic crust during emergence of Nuna. *Lithos*, *278–281*, 427–444. https://doi.org/10.1016/j.lithos.2017.01.029

Krissek, L. (1995). Late Cenozoic ice-rafting records from Leg 145 sites in the North pacific: Late Miocene onset, Late Pliocene intensification, and Pliocene-Pleistocene events. *Proceedings of the Ocean Drilling Program, Scientific Results*, *145*, 179–194. https://doi.org/10.2973/odp.proc.sr.145.118.1995

Lamarque, G., Bascou, J., Ménot, R. P., Paquette, J. L., Couzinié, S., Rolland, Y., & Cottin, J. Y. (2018). Ediacaran to lower Cambrian basement in eastern George V Land (Antarctica): Evidence from U–Pb dating of gneiss xenoliths and implications for the South Australia-East Antarctica connection. *Lithos*, *318–319*, 219–229. https://doi.org/10.1016/j.lithos.2018.08.021

Leitchenkov, G. L. (2015). Environmental and climate changes in Antarctica in the geological past. *Ice and Snow*, *128*(4), 107. https://doi.org/10.15356/2076-6734-2014-4-107-116

Licht, K. J., & Hemming, S. R. (2017). Analysis of Antarctic glacigenic sediment provenance through geochemical and petrologic applications. *Quaternary Science Reviews*, *164*, 1–24. https://doi.org/10.1016/j.quascirev.2017.03.009

Lougheed, B. C., & Obrochta, S. P. (2016). MatCal: Open source Bayesian 14C age calibration in Matlab. *Journal of Open Research Software*, *4*(1), e42. https://doi.org/10.5334/jors.130

Lowry, D. P., Golledge, N. R., Bertler, N. A. N., Jones, R. S., McKay, R., & Stutz, J. (2020). Geologic controls on ice sheet sensitivity to deglacial climate forcing in the Ross Embayment, Antarctica. *Quaternary Science Advances*, *1*, 100002. https://doi.org/10.1016/j.qsa.2020.100002

Ludwig, K. R. (2012). User's manual for Isoplot 3.75, a geochronological toolkit for Microsoft Excel. *Berkeley Geochronology Center Special Publication*, *5*(5), 1–72.

Maritati, A., Halpin, J. A., Whittaker, J. M., & Daczko, N. R. (2019). Fingerprinting Proterozoic Bedrock in interior Wilkes Land, East Antarctica. *Scientific Reports*, *9*(1), 1–12. https://doi.org/10.1038/s41598-019-46612-y

Matthews, K. J., Maloney, K. T., Zahirovic, S., Williams, S. E., Seton, M., & Müller, R. D. (2016). Global plate boundary evolution and kinematics since the late Paleozoic. *Global and Planetary Change*, *146*, 226–250. https://doi.org/10.1016/j.gloplacha.2016.10.002

McDowell, F. W., McIntosh, W. C., & Farley, K. A. (2005). A precise 40Ar-39Ar reference age for the Durango apatite (U-Th)/He and fission-track dating standard. *Chemical Geology*, *214*(3–4), 249–263. https://doi.org/10.1016/j.chemgeo.2004.10.002

Ménot, R. P., Duclaux, G., Peucat, J. J., Rolland, Y., Guillot, S., Fanning, M., et al. (2007). Geology of the terre Adélie craton (135–146°E). *10th International Symposium on Antarctic Earth Sciences*, *1047*, 5. https://doi.org/10.3133/of2007-1047.srp059

Miller, D. S., Duddy, I. R., Green, P. F., Hurford, A. J., & Naeser, C. W. (1985). Results of interlaboratory comparison of fission-track age standards: Fission-track workshop-1984. *Nuclear Tracks and Radiation Measurements (1982)*, *10*(3), 383–391. https://doi.org/10.1016/0735-245X(85)90127-9

Morlighem, M., Rignot, E., Binder, T., Blankenship, D., Drews, R., Eagles, G., et al. (2020). Deep glacial troughs and stabilizing ridges unveiled beneath the margins of the Antarctic ice sheet. *Nature Geoscience*, *13*(2), 132–137. https://doi.org/10.1038/s41561-019-0510-8

Morrissey, L. J., Payne, J. L., Hand, M., Clark, C., Taylor, R., Kirkland, C. L., & Kylander- Clark, A. (2017). Linking the Windmill Islands, east Antarctica and the Albany–Fraser Orogen: Insights from U–Pb zircon geochronology and Hf isotopes. *Precambrian Research*, *293*, 131–149. https://doi.org/10.1016/j.precamres.2017.03.005

Mortlock, R. A., & Froelich, P. N. (1989). A simple method for the rapid determination of biogenic opal in pelagic marine sediments. *Deep Sea Research Part A, Oceanographic Research Papers*, *36*(9), 1415–1426. https://doi.org/10.1016/0198-0149(89)90092-7

Mouginot, J., Scheuchl, B., & Rignot, E. (2017). *MEaSUREs Antarctic boundaries for IPY 2007-2009 from Satellite Radar, Version 2*. Boulder, CO: NASA National Snow and Ice Data Center Distributed Active Archive Center. https://doi.org/10.5067/AXE4121732AD

Mouginot, J., Scheuch, B., & Rignot, E. (2012). Mapping of ice motion in Antarctica using synthetic-aperture radar data. *Remote Sensing*, *4*(9), 2753–2767. https://doi.org/10.3390/rs4092753

Mulder, J. A., Halpin, J. A., Daczko, N. R., Orth, K., Meffre, S., Thompson, J. M., & Morrissey, L. J. (2019). A multiproxy provenance approach to uncovering the assembly of East Gondwana in Antarctica. *Geology*, *47*(7), 645–649. https://doi.org/10.1130/G45952.1

Nelson, D. R., Myers, J. S., & Nutman, A. P. (1995). Chronology and evolution of the middle Proterozoic Albany-Fraser Orogen, western Australia. *Australian Journal of Earth Sciences*, *42*(5), 481–495. https://doi.org/10.1080/08120099508728218

Olierook, H. K. H., Taylor, R. J. M., Erickson, T. M., Clark, C., Reddy, S. M., Kirkland, C. L., et al. (2019). Unravelling complex geologic histories using U–Pb and trace element systematics of titanite. *Chemical Geology*, *504*, 105–122. https://doi.org/10.1016/j.chemgeo.2018.11.004

Orsi, A. H., Whitworth, T., III, & Nowlin, W. D. (1995). On the extent and frontal structure of the Antarctic Circumpolar Current. *Deep-Sea Research Part I*, *2*(43), 96–97.

O'Brien, P. E., Beaman, R., De Santis, L., Domack, E. W., Escutia, C., Harris, P. T., et al. (2016). Submarine glacial landforms on the cold East Antarctic margin. *Geological Society Memoir*, *46*(1), 501–508. https://doi.org/10.1144/M46.172

O'Brien, P. E., Post, A. L., Edwards, S., Martin, T., Caburlotto, A., Donda, F., et al. (2020). Continental slope and rise geomorphology seaward of the Totten Glacier, East Antarctica (112°E-122°E). *Marine Geology*, *427*, 106221. https://doi.org/10.1016/j.margeo.2020.106221

O'Sullivan, G., Chew, D., Kenny, G., Henrichs, I., & Mulligan, D. (2020). The trace element composition of apatite and its application to detrital provenance studies. *Earth-Science Reviews*, *201*, 103044. https://doi.org/10.1016/j.earscirev.2019.103044

Paterne, M., Michel, E., & Héros, V. (2019). Variability of marine 14 C reservoir ages in the Southern Ocean highlighting circulation changes between 1910 and 1950. *Earth and Planetary Science Letters*, *511*, 99–104. https://doi.org/10.1016/j.epsl.2019.01.029

Patterson, M. O., McKay, R., Naish, T., Escutia, C., Jimenez-Espejo, F. J., Raymo, M. E., et al. (2014). Orbital forcing of the east Antarctic ice sheet during the Pliocene and early Pleistocene. *Nature Geoscience*, *7*(11), 841–847. https://doi.org/10.1038/ngeo2273

Pierce, E. L., Hemming, S. R., Williams, T., van de Flierdt, T., Thomson, S. N., Reiners, P. W., et al. (2014). A comparison of detrital U-Pb zircon, 40 Ar/39 Ar hornblende, 40 Ar/39 Ar biotite ages in marine sediments off East Antarctica: Implications for the geology of subglacial terrains and provenance studies. *Earth-Science Reviews*, *138*, 156–178. https://doi.org/10.1016/j.earscirev.2014.08.010

Post, A. L., O'Brien, P. E., Edwards, S., Carroll, A. G., Malakoff, K., & Armand, L. K. (2020). Upper slope processes and seafloor ecosystems on the Sabrina continental slope, East Antarctica. *Marine Geology*, *422*, 106091. https://doi.org/10.1016/j.margeo.2019.106091

Prothro, L. O., Simkins, L. M., Majewski, W., & Anderson, J. B. (2018). Glacial retreat patterns and processes determined from integrated sedimentology and geomorphology records. *Marine Geology*, *395*, 104–119. https://doi.org/10.1016/j.margeo.2017.09.012

Pudsey, C. J. (2000). Sedimentation on the continental rise west of the Antarctic Peninsula over the last three glacial cycles. *Marine Geology*, *167*(3–4), 313–338. https://doi.org/10.1016/S0025-3227(00)00039-6

Rignot, E., Mouginot, J., & Scheuchl, B. (2011). Ice flow of the antarctic ice sheet. *Science*, *333*(6048), 1427–1430. https://doi.org/10.1126/science.1208336

Rignot, E., Mouginot, J., Scheuchl, B., van den Broeke, M., van Wessem, M. J., & Morlighem, M. (2019). Four decades of Antarctic Ice Sheet mass balance from 1979–2017. *Proceedings of the National Academy of Sciences*, *116*(4), 1095–1103. https://doi.org/10.1073/pnas.1812883116

Roy, M., van de Flierdt, T., Hemming, S. R., & Goldstein, S. L. (2007). 40Ar/39Ar ages of hornblende grains and bulk Sm/Nd isotopes of circum-Antarctic glacio-marine sediments: Implications for sediment provenance in the southern ocean. *Chemical Geology*, *244*(3–4), 507–519. https://doi.org/10.1016/j.chemgeo.2007.07.017

Rubatto, D. (2017). Zircon: The metamorphic mineral. *Reviews in Mineralogy and Geochemistry*, *83*(1), 261–295. https://doi.org/10.2138/rmg.2017.83.9

Schmitz, M. D., & Bowring, S. A. (2001). U-Pb zircon and titanite systematics of the Fish Canyon Tuff: An assessment of high-precision U-Pb geochronology and its application to young volcanic rocks. *Geochimica et Cosmochimica Acta*, *65*(15), 2571–2587. https://doi.org/10.1016/S0016-7037(01)00616-0

Schoene, B., & Bowring, S. A. (2006). U-Pb systematics of the McClure Mountain syenite: Thermochronological constraints on the age of the 40Ar/39Ar standard MMhb. *Contributions to Mineralogy and Petrology*, *151*(5), 615–630. https://doi.org/10.1007/s00410-006-0077-4

Shao, T., Xia, Y., Ding, X., Cai, Y., & Song, M. (2019). Zircon saturation in terrestrial basaltic melts and its geological implications. *Solid Earth Sciences*, *4*(1), 27–42. https://doi.org/10.1016/j.sesci.2018.08.001

Sláma, J., Košler, J., Condon, D. J., Crowley, J. L., Gerdes, A., Hanchar, J. M., et al. (2008). Plešovice zircon—A new natural reference material for U-Pb and Hf isotopic microanalysis. *Chemical Geology*, *249*(1–2), 1–35. https://doi.org/10.1016/j.chemgeo.2007.11.005

Spaggiari, C. V., Kirkland, C. L., Smithies, R. H., Wingate, M. T. D., & Belousova, E. A. (2015). Transformation of an Archean craton margin during Proterozoic basin formation and magmatism: The Albany-Fraser Orogen, Western Australia. *Precambrian Research*, *266*, 440–466. https://doi.org/10.1016/j.precamres.2015.05.036

Spaggiari, C. V., Smithies, R. H., Kirkland, C. L., Wingate, M. T. D., England, R. N., & Lu, Y. J. (2018). Buried but preserved: The Proterozoic Arubiddy ophiolite, Madura province, western Australia. *Precambrian Research*, *317*, 137–158. https://doi.org/10.1016/j.precamres.2018.08.025

Stacey, J. S., & Kramers, J. D. (1975). Approximation of terrestrial lead isotope evolution by a two-stage model. *Earth and Planetary Science Letters*, *26*(2), 207–221. https://doi.org/10.1016/0012-821X(75)90088-6

Sun, S. S., & McDonough, W. F. (1989). Chemical and isotopic systematics of oceanic basalts: Implications for mantle composition and processes. *Geological Society—Special Publications*, *42*(1), 313–345. https://doi.org/10.1144/GSL.SP.1989.042.01.19

Thompson, J. M., Meffre, S., & Danyushevsky, L. (2018). Impact of air, laser pulse width and fluence on U-Pb dating of zircons by LA-ICPMS. *Journal of Analytical Atomic Spectrometry*, *33*(2), 221–230. https://doi.org/10.1039/c7ja00357a

Thompson, J., Meffre, S., Maas, R., Kamenetsky, V., Kamenetsky, M., Goemann, K., et al. (2016). Matrix effects in Pb/U measurements during LA-ICP-MS analysis of the mineral apatite. *Journal of Analytical Atomic Spectrometry*, *31*, 1206–1215. https://doi.org/10.1039/c6ja00048g

Tucker, N. M., Payne, J. L., Clark, C., Hand, M., Taylor, R. J. M., Kylander-Clark, A. R. C., & Martin, L. (2017). Proterozoic reworking of Archean (Yilgarn) basement in the bunger Hills, east Antarctica. *Precambrian Research*, *298*, 16–38. https://doi.org/10.1016/j.precamres.2017.05.013

Veevers, J. J. (2012). Reconstructions before rifting and drifting reveal the geological connections between Antarctica and its conjugates in Gondwanaland. *Earth-Science Reviews*, *111*(3-4), 249–318. https://doi.org/10.1016/j.earscirev.2011.11.009

Veevers, J. J., & Saeed, A. (2011). Age and composition of Antarctic bedrock reflected by detrital zircons, erratics, and recycled microfossils in the Prydz Bay-Wilkes Land-Ross Sea-Marie Byrd Land sector (70°-240°E). *Gondwana Research*, *20*(4), 710–738. https://doi.org/10.1016/j.gr.2011.03.007

Vermeesch, P. (2018). IsoplotR: A free and open toolbox for geochronology. *Geoscience Frontiers*, *9*(5), 1479–1493. https://doi.org/10.1016/j.gsf.2018.04.001

Weber, M. E., Clark, P. U., Kuhn, G., Timmermann, A., Sprenk, D., Gladstone, R., et al. (2014). Millennial-scale variability in Antarctic ice-sheet discharge during the last deglaciation. *Nature*, *510*(7503), 134–138. https://doi.org/10.1038/nature13397

Williams, T., van de Flierdt, T., Hemming, S. R., Chung, E., Roy, M., & Goldstein, S. L. (2010). Evidence for iceberg armadas from East Antarctica in the Southern Ocean during the late miocene and early Pliocene. *Earth and Planetary Science Letters*, *290*(3–4), 351–361. https://doi.org/10.1016/j.epsl.2009.12.031

Williams, S. E., Whittaker, J. M., Halpin, J. A., & Müller, R. D. (2019). Australian-Antarctic breakup and seafloor spreading: Balancing geological and geophysical constraints. *Earth-Science Reviews*, *188*, 41–58. https://doi.org/10.1016/j.earscirev.2018.10.011

Wilson, D. J., Bertram, R. A., Needham, E. F., van de Flierdt, T., Welsh, K. J., McKay, R. M., et al. (2018).Ice loss from the east antarctic ice sheet during late pleistocene interglacials. *Nature*, *561*(7723), 383–386. https://doi.org/10.1038/s41586-018-0501-8

Wingate, M. T. D., Kirkland, C. L., & Smithies, R. H. (2015). U-Pb geochronology of the Forrest Zone of the Coompana Province. In C. V. Spaggiari & R. H. Smithies (Eds.), *Eucla basement stratigraphic drilling results release workshop: Extended abstracts compiled* (pp. 37–40). Geological Survey of Western Australia Record 2015/10.

Wingate, M. T. D., Kirkland, C. L., Spaggiari, C. V., & Smithies, R. H. (2015). U-Pb geochronology of the Madura province. In C. V. Spaggiari & R. H. Smithies (Eds.), *Eucla basement stratigraphic drilling results release workshop: Extended abstracts compiled*, 10, 14–16). Perth, WA: Geological Survey of Western Australia Record 2015/10.

Young, D. A., Wright, A. P., Roberts, J. L., Warner, R. C., Young, N. W., Greenbaum, J. S., et al. (2011). A dynamic early East Antarctic Ice Sheet suggested by ice-covered fjord landscapes. *Nature*, *474*(7349), 72–75. https://doi.org/10.1038/nature10114